

Spontaneous phase locking in a broad-area semiconductor laser

Stefan Bittner^{1,2,*} and Marc Sciamanna^{1,2}

¹*Chaire in Photonics, LMOPS, CentraleSupélec, 2 rue Edouard Belin, 57070 Metz, France*

²*Université de Lorraine, CentraleSupélec, LMOPS, 2 rue Edouard Belin, 57070 Metz, France*

(Dated: May 14, 2024)

Broad-area semiconductor lasers are employed in many high-power applications, however, their spatio-temporal dynamics is complex and intrinsically unstable due to the interaction of several transverse lasing modes. A dynamical and spatio-spectral analysis with ultra-high resolution of commercial broad-area lasers reveals multiplets of phase locked first- and second-order transverse modes that are spontaneously created by the nonlinear dynamics for a wide range of operation parameters. Phase locking between modes of different transverse order is demonstrated by comparing the linewidths of the lasing modes to that of their beat note as well as by a direct measurement of their phase fluctuation correlations. Since the laser and the setup lack any feature designed to induce locking and the overall dynamics is unstable, the observation of this spontaneous phase locking effect is very unexpected. Our findings indicate that chimera-like states featuring groups of synchronized oscillators coexisting with unsynchronized ones can spontaneously form in broad-area lasers, and may thus be found in a wider range of optical systems and beyond than previously assumed. Moreover, some of the phase locked modes do not even exist on the passive-cavity level, but are created by the nonlinear dynamics, an effect not previously observed in the context of chimera states.

I. INTRODUCTION

The dynamics of lasers is very rich, ranging from stable emission and periodic dynamics to deterministic chaos [1–4]. Moreover, spatial pattern formation and complex spatio-temporal dynamics are observed for lasers featuring several transverse modes [5, 6], for example in gas lasers [7], fiber lasers [8, 9] and both surface-emitting [10, 11] and edge-emitting [12–14] semiconductor lasers. Such broad-area lasers (BALs) are needed to reach very high output powers beyond the limitations of single transverse-mode lasers. However, they are susceptible to spatio-temporal instabilities stemming from the interaction of different transverse lasing modes. While progress has been made in controlling spatio-temporal dynamics with special device designs [15–20], the understanding or even just documentation of dynamical phenomena occurring in generic broad-area lasers remains far from complete.

Beyond application-related considerations, BALs are hence interesting model systems for studying complex multimode dynamics. Important issues are the possibly chaotic nature of the spatio-temporal dynamics, how lasing modes organize in space, wavelength and time, and if synchronization or other forms of collective dynamics of lasing modes occur. An interesting form of collective dynamics are so-called chimera states [21, 22] in which groups of synchronized oscillators coexist with a large number of unsynchronized ones. Chimera states have been predicted numerically for arrays of coupled lasers [23] and demonstrated experimentally for semiconductor lasers with feedback [24, 25] and absorptive sections [26]. Similarly, synchronization of mode clusters was found for

quantum dot [27] and quantum cascade [28] lasers. However, previous works concerned only lasers with a single transverse mode, whereas cluster synchronization of different transverse modes has not been studied before.

We investigate a broad-area edge-emitting semiconductor laser with a quantum well as active medium. Semiconductor BALs suffer from filamentation, which is an intrinsic spatio-temporal instability caused by the combination of spatial-hole burning, carrier-induced index changes and diffraction [12, 13, 29–32]. Filamentation is sometimes attributed to (partial) self-mode locking [30, 33, 34], and mode-locking between longitudinal and transverse modes can be induced by pulsed optical injection [33, 34]. However, phase- or mode-locking effects in normal, free-running quantum-well BALs have never been experimentally demonstrated even though they could explain the significant long-range correlations of the spatio-temporal dynamics [12, 29, 35, 36].

We perform dynamical and spatio-spectral measurements with ultra-high resolution in order to identify the different transverse modes and find possible correlations between them. We observe a previously undocumented dynamical effect, the creation of multiplets of 1st- and 2nd-order transverse modes which are phase locked and that coexist with many unlocked modes. This chimera-like state is observed for two different lasers and in a wide range of operation parameters.

II. EXPERIMENTAL RESULTS

We investigate a commercial broad-area laser (see Appendix A 1) with continuous wave pumping in solitary operation, i.e., without optical injection, feedback or modulation. The lateral confinement in the 50 μm wide and 1.5 mm long cavity is due to a combination of gain and

* stefan.bittner@centralesupelec.fr

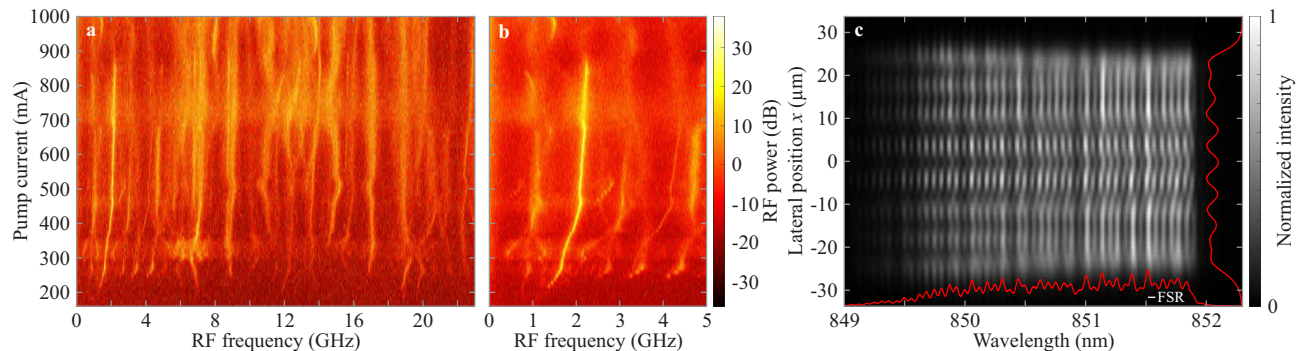


FIG. 1. **Emission properties of the BAL.** **a**, RF-spectra of the total laser emission and **b** magnification around the particularly narrow frequency component near 2 GHz. **c**, Spatio-spectral near-field image at 1000 mA and its spatial and spectral projections (red). The small white bar indicates the free spectral range.

index guiding, and the laser threshold is $I_{th} = 160$ mA.

Figure 1a shows the RF-spectra of the BAL as function of pump current. They were measured by coupling the complete laser beam into a multimode fiber connected to a fast photodetector (see Appendix A 2). The laser shows significant instabilities, and the RF-spectra feature a number of discrete and partially overlapping peaks on a broad background. The peaks typically have linewidths (FWHM) of 100 MHz or more. However, one peak around 2 GHz is significantly narrower (see magnification in Fig. 1b) with a linewidth below 10 MHz for pump currents up to 600 mA. It becomes broader and disappears as the pump current increases further (see Fig. 10). We surmise that the peaks in the RF-spectra are beat notes between different lasing modes [37], in which case the narrow peak could be explained by the beating of phase locked modes.

In order to confirm this, we performed spatio-spectral measurements using an imaging spectrometer with 30 pm resolution (see Appendix A 2). The spatio-spectral image for 1000 mA in Fig. 1c shows spatial patterns varying with the wavelength due to the presence of several transverse modes. The spectrally-integrated near-field intensity distribution has a top-hat profile with regular modulation which indicates the presence of high-order transverse modes (see Fig. 6 for more details). The spatially integrated spectrum shows only a single series of peaks with the longitudinal-mode spacing (free spectral range, FSR) of 25.9 GHz, effectively hiding the presence of several transverse modes (see Fig. 5). More sophisticated grating-based setups enable spatio-spectral measurements with resolutions as good as 120 MHz [38–40], which is sufficient to resolve the different transverse modes. However, in order to detect phase locking effects, we also need to measure the linewidths of the lasing modes which are of the order of 100 MHz for multimode semiconductor lasers [41]. Hence, we adopt a heterodyne technique that permits even better spectral resolution [37, 42, 43] and measuring the phases of lasing modes [44].

In order to perform spatially-resolved heterodyne mea-

surements, we collect the BAL emission in the image plane of its output facet with a multimode fiber (MMF) whose lateral position is scanned (see Fig. 7). The signal of the BAL interferes with a single-mode reference laser on a fast photodetector to create beat notes from which we reconstruct the optical spectrum of the BAL (see Appendix B). The spectral resolution of the heterodyne measurement is fundamentally limited by the linewidth of the reference laser, which is < 1 MHz.

We first consider a pump current of 1000 mA, which is a current regime without narrow peak in the RF-spectrum. The reconstructed spatio-spectral image (see Appendix B 2) in Fig. 2 covers almost two FSRs and features transverse modes of order $q = 1-8$, where $q = 1$ is the fundamental mode. Since the spacing between the 1st-order transverse mode and those with $q = 6-8$ is larger than the FSR, different longitudinal-mode groups mix, and the modes with $q = 3, 6$ and 8 are spectrally close as a consequence. The linewidths of the lasing modes (Fig. 2b) are in the range of 50–300 MHz.

Figure 2c presents typical mode profiles, which show significant deviations from those expected in a passive Fabry-Perot (FP) cavity. First, the fundamental mode $q = 1$ has a dip in the center and thus two peaks instead of one, in contrast to observations for other devices [38, 39, 45]. Second, the peak heights are not uniform. For example, the $q = 3$ and 8 modes have a higher peaks in the center, whereas the $q = 7$ mode has an envelope with a dip in the center. Third, several modes have asymmetries even though the spectrally-integrated near-field intensity distributions are symmetric (see Fig. 6). In particular, the right (left) peak of the 1st (2nd) order mode is always higher. Thus, these two modes have complementary profiles as if they were competing for gain. It should be noted that the features discussed above are systematically found in all measurements. In a cavity with only index guiding in the lateral direction, the peak heights would of course be homogeneous [39], but an inhomogeneous current density as well as thermal lensing effects can significantly modify the mode profiles. In Ref. [39],

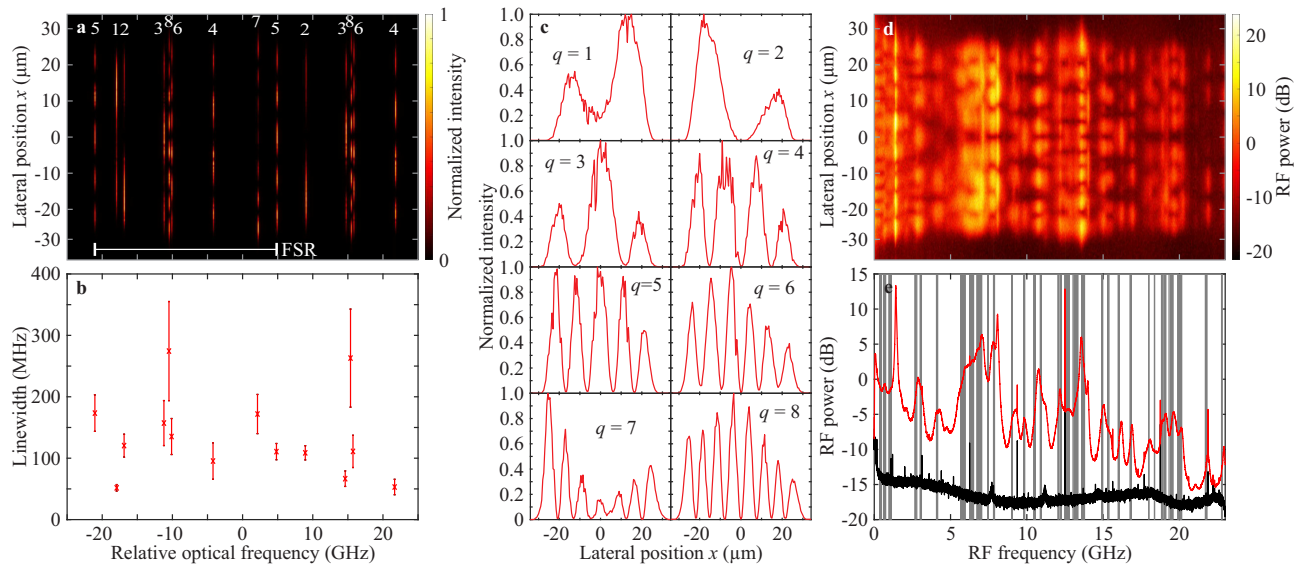


FIG. 2. **Heterodyne measurement results at 1000 mA.** **a**, Reconstructed spatio-spectral image around a reference wavelength of 851.142 nm. The white numbers indicate the transverse quantum numbers of the modes, and the white bar the FSR. **b**, Linewidths of the lasing modes. **c**, Typical mode profiles for modes with transverse quantum numbers $q = 1-8$. **d**, Spatially resolved RF-spectrum. **e**, Spatially-averaged RF-spectrum (red) and detector background signal (black). The vertical gray lines indicate the beat frequencies of the lasing modes.

thermal lensing was found to be the dominant mechanism, though no explanation for the observed asymmetries was given. Dynamical effects like spatial and spectral hole burning can play an important role as well.

The spatially-resolved RF-spectrum in Fig. 2d shows that different frequency components exhibit different spatial patterns, which is expected if they result from beating of different transverse modes [37]. Figure 2e compares the spatially-averaged RF-spectrum (red line) to the beat notes (i.e., optical frequency differences) of the lasing modes (vertical gray lines) obtained from six heterodyne measurements at 1000 mA. Almost all major peaks and frequency components in the RF-spectrum can thus be explained as beat notes. The widths of the peaks in the RF-spectrum (typically 100 MHz and more) are also consistent with the widths of the lasing modes (see Fig. 2b). However, the significant offset of the RF-spectrum compared to the background signal (black line) over the whole frequency range as well as a few unexplained peaks indicate that dynamical effects beyond mode beating could contribute as well.

In conclusion, the experimental results for high pump currents are not unusual for a semiconductor BAL, even though some aspects of the RF-spectra and mode profiles merit further analysis. Now we turn our attention to lower pump currents to elucidate the creation of a narrow RF-peak by spontaneously phase-locked multiplets.

The spatio-spectral image for 350 mA in Fig. 3a shows transverse modes up to order $q = 6$. Surprisingly, we observe a quintuplet and a triplet of 1st- and 2nd-order modes (indicated by the green boxes), that is, additional

lasing modes are created by the nonlinear dynamics. The schematic representation of the quintuplet in Fig. 3b shows two 1st-order modes followed by two 2nd-order modes and a fifth mode whose spatial profile does not allow a clear identification. Many such multiplets are found for 300 to 650 mA, always consisting of modes with $q = 1$ and 2, but also longitudinal mode groups with only one transverse mode of each order like for higher pump currents are observed. Most examples are triplets, though it is possible that sometimes weaker modes in the multiplets were not detected.

Interestingly, the nearest-neighbor (NN) spacings indicated in Fig. 3b are not equal, instead, every second spacing is different. This means that four-wave mixing cannot be responsible for creating the multiplets since it would result in equidistant modes. More importantly, the next-nearest-neighbor (NNN) spacings are all the same and equal to the frequency of the narrow peak in the RF-spectrum highlighted in Fig. 1b. In other words, this peak results from the beating of pairs of modes with different transverse order of which one was created by nonlinear laser dynamics. Figure 3c shows perfect agreement between the frequency of the peak in the RF-spectra (black line) and the NNN spacings (red) in the current range of interest.

The frequency of this narrow beat note has a complicated dependency on pump current and temperature (see Fig. 10). It increases significantly with the pump current, but does not exhibit the square-root scaling of the relaxation oscillation frequency. It is of the same order as two times the NN spacing between 1st- and 2nd-order modes

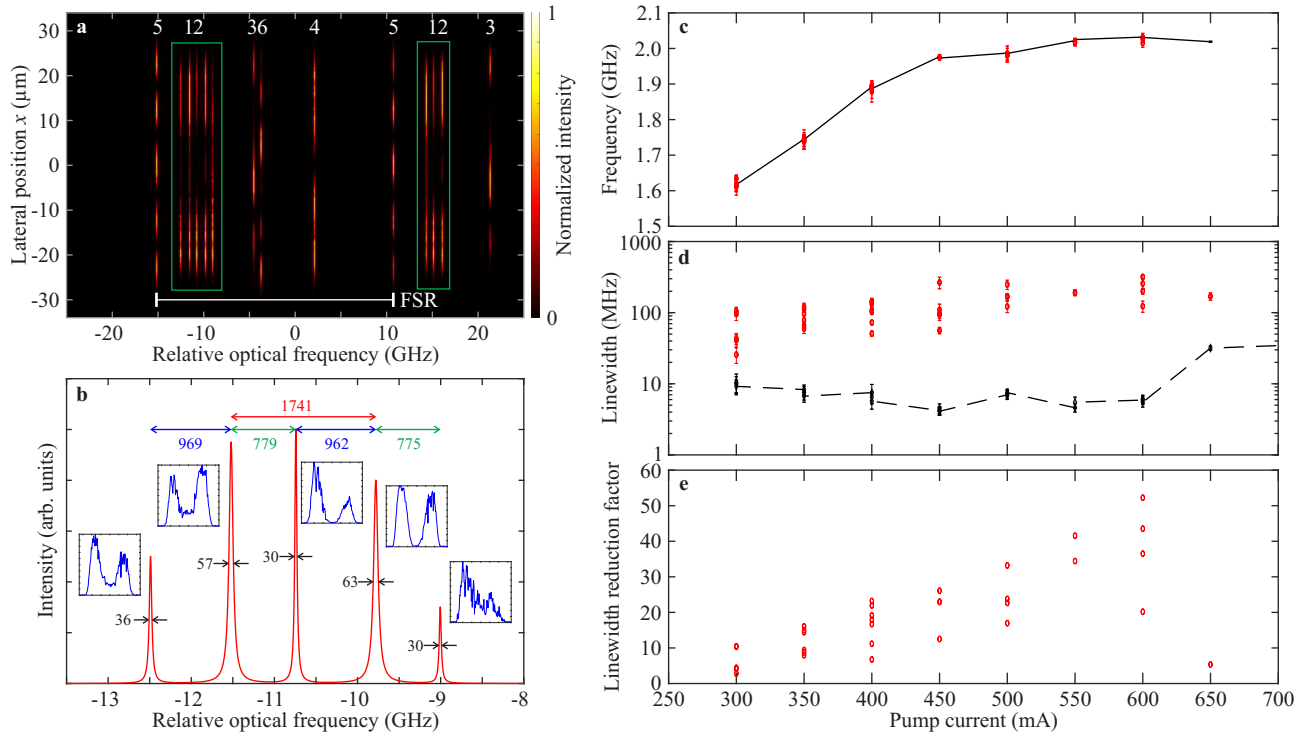


FIG. 3. **Heterodyne measurement results at 350 mA.** **a**, Reconstructed spatio-spectral image around a reference wavelength of 849.594 nm. The green boxes mark a quintuplet and a triplet of 1st- and 2nd-order modes. **b**, Schematic of the quintuplet. The insets show the spatial profiles of the different modes, and the black arrows indicate their linewidths. The spacings and linewidth are given in MHz. **c**, Frequency of the narrow peak in the RF-spectrum (black) and NNN-spacings of multiplets (red) as function of the pump current. **d**, Linewidth of the narrow peak (black) and sum of linewidths of NNN-mode pairs. **e**, Linewidth reduction factor for different NNN-mode pairs.

which increases with pump current (see Fig. 12).

The linewidths of the lasing modes in the quintuplet are indicated by the double arrows in Fig. 3b. Every second mode has a clearly larger linewidth than its neighbors (see also Fig. 13). More importantly, the mode linewidths are significantly larger than that of the beat note, which is smaller than 10 MHz in the regime up to 600 mA (black symbols in Fig. 3d). If the phase fluctuations of the lasing modes were independent, the linewidth of their beat note would be equal to the sum of their linewidths (see Appendix D 1). Instead, the sum of the linewidths of the NNN-mode pairs (red symbols) is of the order of 100 MHz in most cases. So the linewidth of the beat note is typically reduced by a factor (called linewidth reduction factor, LRF) ranging from 10 to 50 compared to the sum of the mode linewidths as shown in Fig. 3e. This means that the phase fluctuations of the NNN-mode pairs are highly correlated, i.e., these lasing modes are phase locked. This spontaneous phase locking is surprising since the BAL is in solitary operation without feedback, injection [33, 34], modulation or saturable absorbers [26]. It should be noted that the LRF shown in Fig. 3e increases till 600 mA, i.e., the phase locking gets stronger, until it is lost around 650 mA where the beat note becomes broader again (see also Fig. 10).

The analysis of the linewidths is not a proof of phase locking of particular mode pairs since (i) it is not clear which NNN-mode pairs in the multiplets are phase locked or not and (ii) we cannot exclude the existence of mode pairs with narrow linewidths in other longitudinal mode groups that could explain the narrow beat note without phase locking. Furthermore we wonder if the NN-mode pairs may be weakly phase locked even though their beat note is not particularly narrow. Fortunately we can obtain direct proof of phase fluctuation correlations (PFCs) between different modes from the time-domain measurements of the heterodyne signals.

The analysis to extract the phase fluctuations of lasing modes and calculate their correlations is explained in Appendix D. Figure 4(a) shows the PFC matrix for the lasing modes presented in Fig. 3, where the quintuplet and triplet are marked by green boxes. Most mode pairs exhibit negligibly small correlations, whereas significant correlations are observed between the modes of the multiplets. The highest correlations are found for NNN-mode pairs (second off-diagonal), all of which are clearly correlated. There are also correlations between the NN-mode pairs (first off-diagonal), but they are weaker. Moreover, it should be noted that some correlations are found between the modes of the quintuplet and the triplet which

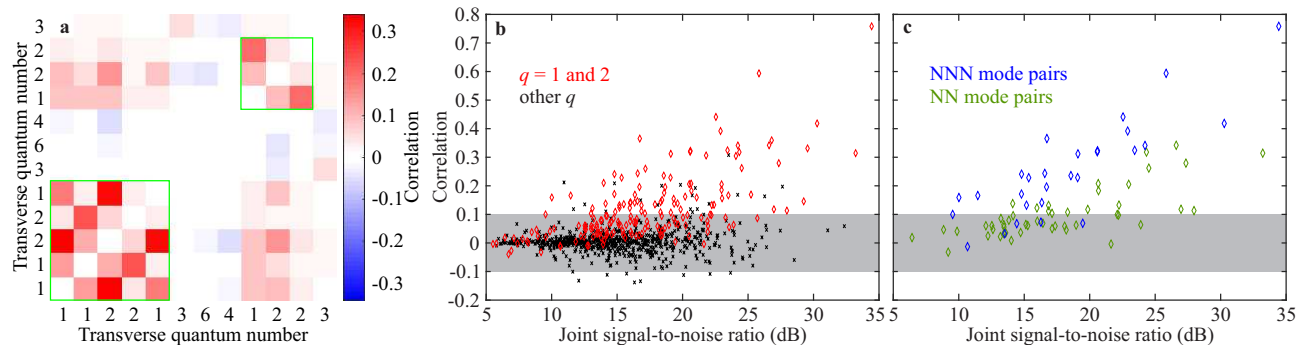


FIG. 4. **Phase fluctuation correlations.** **a**, Matrix of phase fluctuation correlations for the measurement shown in Fig. 3a. The green boxes indicate the quintuplet and the triplet. **b**, Phase fluctuation correlations as function of the joint signal-to-noise ratio for all mode pairs in data sets with multiplets. Pairs of first- and second-order modes are indicated in red, all other pairs in black. The gray rectangle indicates the range of not significant correlations of ± 0.1 . **c**, Phase fluctuation correlations of NN-mode pairs (green) and NNN-mode pairs (blue) only.

are one FSR away. These findings are exemplary for all the multiplets we found and are consistent with the linewidths of lasing modes and their beat notes as discussed above. They clearly prove that the modes created by the nonlinear dynamics are phase locked to their next-nearest neighbors, which suggests that a coherent effect is responsible for their creation.

However, the measured PFCs are lower than could be expected from the linewidth reduction factors shown in Fig. 3e. For example, a LRF of 10 corresponds to a PFC of 0.9 (see Fig. 14), but such high values are not observed. In fact, the calculation of the PFCs is very sensitive to perturbations by measurement noise and interfering signals from the BAL dynamics. Figure 4b shows the PFCs of all measurements featuring multiplets as function of the joint signal-to-noise ratio (SNR), which is the mean of the SNRs of the two heterodyne signals (see Appendix D 3 for details). We see a clear increase of the maximal observed PFCs with the joint SNR. Hence, one should compare the PFC of a mode pair to that of other mode pairs with the same joint SNR in order to determine if the PFC can be considered high or not.

Most mode pairs in Fig. 4 have PFCs in the range of ± 0.1 , which we consider as not significant and the involved modes as effectively uncorrelated. The comparison of correlations between modes of 1st and 2nd order (i.e., pairs with transverse quantum numbers (1, 1), (1, 2) or (2, 2), indicated in red) to all other mode pairs (indicated in black) shows that only the modes with $q = 1$ and 2 exhibit significant correlations, with a few exceptions to be discussed elsewhere. Figure 4c shows only the PFCs of NN- and NNN-mode pairs in multiplets, where the NNN-correlations are systematically higher than the NN-correlations for a given joint SNR. This confirms that the phase locking between NNN-modes is stronger compared to NN-pairs.

III. DISCUSSION

Our experiments reveal a spontaneous phase locking of transverse modes in a simple broad-area Fabry-Perot cavity without special features or external control elements. This is surprising given the significant spatio-temporal instabilities of such devices. Since only two out of up to eight transverse mode orders are phase locked, the dynamics of the BAL remains complex and unstable. Hence the phase-locking effect is not easily recognized, and direct measurements of the phase fluctuation correlations are needed to ascertain which modes are locked.

Mode locking can be induced by various techniques including saturable absorbers, external modulation and feedback. Longitudinal [33] and transverse mode-locking [34] in broad-area lasers has also been induced via pulsed injection. Furthermore, spatio-temporal mode locking has been demonstrated for Helium-Neon lasers [46], Ti:Sapphire lasers [47] and fiber lasers [15, 16], but requires careful design of the laser system and its cavity. In our case, in contrast, phase locked multiplets emerge *spontaneously* from the internal laser dynamics of a BAL with a normal Fabry-Perot cavity. While spontaneous phase, frequency and mode locking have been observed before for semiconductor lasers, our case is different to previous works in several respects as discussed in the following.

For semiconductor lasers with relatively narrow FP cavities featuring only the 1st- and 2nd-order transverse modes, phase locking between the transverse modes has been observed [48], which leads to a periodic oscillation of the beam profile, as well as frequency locking [49, 50], which results in asymmetric, static emission profiles and beam steering. Phase locking [51, 52] and frequency locking [53, 54] between two different spatial modes have also been observed for asymmetric cavities. However, in these examples only two different spatial modes lase in the first place, whereas our BAL features up to 8 transverse lasing

modes. Moreover, only modes that naturally exist in the passive cavity were locked, whereas we observe multiplets of modes newly created by the nonlinear dynamics.

Quantum cascade lasers (QCLs) can exhibit spontaneous mode locking between longitudinal modes [55, 56]. Furthermore, QCL frequency combs with phase and frequency locking of several transverse modes have been demonstrated [57, 58]. However, the dynamics of QCLs is quite different from that of quantum well lasers due to the much shorter gain recovery time and the strong third-order nonlinearity [55] of the former. Locking processes in QCLs are mainly attributed to four-wave mixing, whereas, as we concluded earlier, the creation and phase locking of transverse modes presented here cannot be explained by four-wave mixing.

The most interesting aspect of our laser is the coexistence of groups of coherent modes (the phase locked multiplets) with a large number of incoherent (not phase locked) modes, reminiscent of chimera states [21, 22]. Chimera states have been reported for semiconductor lasers with feedback [24, 25], in which case virtual oscillators in the feedback loop are considered instead of actual lasing modes like in our case. Spontaneous synchronization of mode clusters was found for a quantum dot laser [27], but the synchronization concerned the amplitude dynamics of different longitudinal modes, not the phases. Cluster synchronization was furthermore found among the longitudinal modes of a semiconductor laser with absorbing section [26], and among the beat notes of a QCL with tunable mirror reflectivity [28]. While Refs. [26–28] show synchronization between different longitudinal modes, which can be considered as identical oscillators, we demonstrate for the first time spontaneously-formed mode clusters with different transverse modes, that is, clusters of non-identical oscillators. More importantly, in our case the nonlinear dynamics is not only responsible for coupling different oscillators as in previous works, but it moreover creates additional oscillators that are not present in the system *a priori*.

The observation of groups of phase locked modes in a commercial semiconductor laser indicates that cluster synchronization and chimera states may be more frequent in lasers and other nonlinear systems than previously thought. The spatio-temporal dynamics of broad-area lasers is still not fully understood, and our observation of spontaneous phase locking gives a new perspective for understanding and possibly controlling their instabilities using, e.g., optical injection or special cavity designs. This will have important implications for our fundamental understanding of complex spatio-temporal and multimode dynamics as well as for applications like mode-locked lasers.

ACKNOWLEDGMENTS

The Chair in Photonics is supported by Région Grand Est, GDI Simulation, Département de la Moselle, Euro-

pean Regional Development Fund, CentralSupélec, Fondation CentralSupélec, and the Eurometropole de Metz. S.B. thanks Mario Fernandes for technical support.

Appendix A: Experimental setup and basic measurements

1. Broad-area laser

We use a commercial quantum-well semiconductor laser from Shearman (P/N CM-850-1000-050) mounted on a C-mount. The cavity is laterally defined by etching to just above the active layer and depositing a dielectric afterwards, which gives the laser an aspect of both gain and index guiding. The laser is operated in a temperature-controlled laser diode mount (Thorlabs LDMC20/M) and pumped in continuous wave operation by a diode driver (Thorlabs ITC4005). The temperature of the mount is kept constant at 21°C during all measurements unless otherwise noted. The laser emission is transverse-electric polarized (electric field parallel to the cavity plane).

2. Time-domain and spectral measurements

Time-domain measurements were performed with a fast photodetector (Newport 1484-A-50, 15 kHz to 22 GHz) connected to a traveling-wave amplifier (Newport 1421, 8.5 dB) and an oscilloscope (Tektronix DPO72304SX, 23 GHz). Time traces were measured with 50 GSamples/s (20 ps time step) and 10^6 points (20 μ s long). RF-spectra were obtained by calculating the Fourier transform of the time traces and were smoothed with a 2 MHz wide moving average. It should be noted that extremely narrow peaks are observed in many RF-spectra: these are artifacts due to synchronization issues between different analog-to-digital converters of the oscilloscope and appear even without input signal. Hence they have no physical significance and should be ignored.

For measurements of the total laser emission, the beam was coupled into a graded-index multimode fiber (MMF, 50 μ m diameter, NA= 0.20, Thorlabs M116L02) using a 20 \times aspheric objective lens (Newport 5724-B-H, NA = 0.5) in a fiber coupler. Feedback from reflections at the fiber facet were avoided via an optical isolator (OI, Thorlabs IO-5-850-VLP). The multimode fiber was connected to the photodetector or the OSA. It should be noted that coupling the beam of a multi-transverse mode laser into a single-mode fiber is very inefficient, and more importantly the higher-order transverse modes have a lower coupling efficiency compared to low-order modes, which results in an observational bias.

Spatio-spectral images with low resolution (Fig. 1c) were obtained with an imaging spectrometer (Princeton

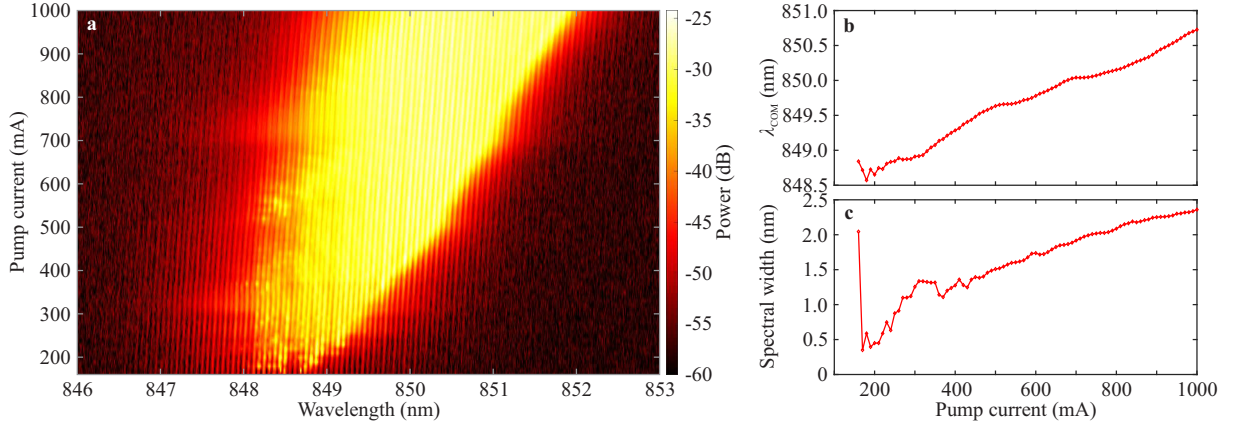


FIG. 5. **Spectra of total laser emission measured with an OSA.** **a**, Spectra of the BAL as function of the pump current. **b**, Center-of-mass wavelength λ_{COM} . **c**, Width of spectra.

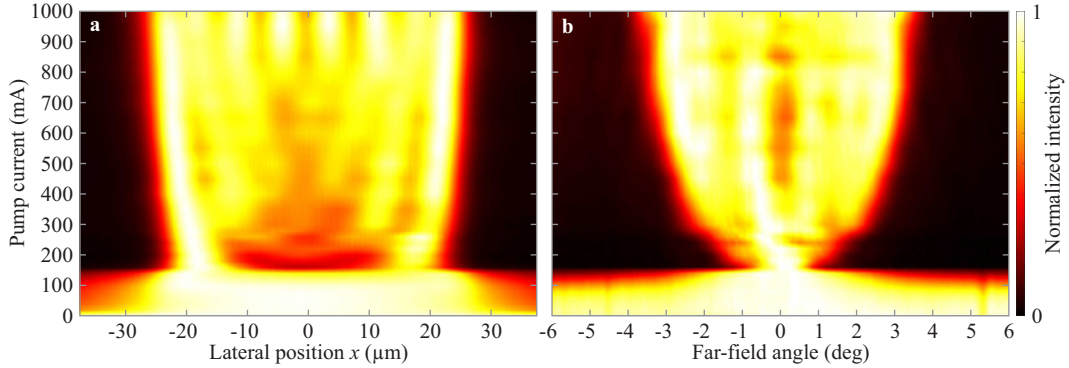


FIG. 6. **Near- and far-field intensity distributions.** **a**, Near-field images. **b**, Far-field images. The intensity distributions for each pump current are normalized to unit amplitude.

Instruments SpectraPro HRS-500 with 1800 g/mm grating, 30 pm resolution) and a CCD camera (Allied Vision Mako U-503B). In order to measure the spectrally-resolved near-field intensity distributions, the output facet of the BAL was imaged onto the entrance slit of the spectrometer with $40\times$ magnification. A dove prism (Thorlabs PS992M-B) was used to rotate the image of the BAL facet by 90° so it matches the vertical orientation of the entrance slit.

3. Low-resolution optical spectra

Figure 5 shows low-resolution lasing spectra of the BAL measured with an optical spectrum analyzer (OSA, Anritsu MS9740A) with 30 pm resolution (12.5 GHz). While the spectral resolution of the OSA is relatively low, it allows measurements over a broader spectral range than the heterodyning technique. At low resolution, the spectra feature a single series of peaks with spacing equal to the free spectral range (FSR) of 25.9 GHz (62.4 pm), hiding the fact that the laser exhibits several transverse

modes. As the pump current increases, the center of mass (COM) of the spectrum red-shifts (see Fig. 5b) due to Joule heating. The total shift is about 2 nm over 800 mA. The red-shift of the individual peaks in the spectrum can also be seen in 5a.

The width of the spectrum, here given by the participation ratio

$$\left[\int d\lambda P(\lambda) \right]^2 / \int d\lambda P^2(\lambda) \quad (\text{A1})$$

where $P(\lambda)$ is the optical power measured by the OSA, increases from 0.35 nm just above threshold to 2.36 nm at 1000 mA, which corresponds to about 38 longitudinal mode groups. With 8 transverse modes, we estimate that the BAL emits in up to 300 lasing modes in parallel, though the actual number is not clear and may be lower since not every transverse mode is found in every longitudinal mode group.

4. Near- and far-field intensity distributions

The output facet of the BAL is imaged onto a CMOS camera (Allied Vision Mako U-503B) using a $25\times$ microscope objective (NA = 0.5) and a lens with 175 mm focal length (Thorlabs LA1399-B) in a telescope configuration. A beam splitter and third lens (Thorlabs LA1050-B, 100 mm focal length) are used to obtain the Fourier transform of the image plane for parallel far-field measurements with a second camera (Allied Vision Mako U-130B). The far-field angle is calculated from the magnification of the telescope and the focal length of the third lens. Neutral-density filters in the beam path and the exposure times of the cameras are adjusted during the measurement to avoid both low signal strength and saturation.

Figure 6a shows the measured near-field intensity distributions, which are almost uniformly flat well below threshold ($I_{th} = 160$ mA). Just above threshold, the intensity distribution exhibits a strong dip in the center with two peaks near the edges of the output facet. As the pump current increases, these two peaks move further towards the edges, and the center of the intensity distribution slowly fills. Above approximately 850 mA the near-field distribution develops a top hat profile with significant modulation (see Fig. 1b). A similar evolution of the near-field intensity distributions as function of the pump current was observed in Ref. [59] and attributed to the interplay of index guiding and carrier-induced index changes. It should be noted that the near-field images are very symmetric around $x = 0$ even though the individual transverse mode profiles show significant asymmetries.

The far-field intensity distributions shown in Fig. 6b are very broad below threshold and collapse to a single lobe at 0° just above threshold. In this current regime, mainly the 1st- and 2nd-order modes lase, but the near-field distributions exhibit a pronounced dip in the center nonetheless since the fundamental mode features a trough like the $q = 2$ mode (see Fig. 2c). As the pump current increases, higher-order modes start to lase, and the power shifts away from the low order modes.

Appendix B: Spatially-resolved heterodyne measurements

1. Experimental setup and measurement protocol

Figure 7 shows the experimental setup for spatially-resolved heterodyne measurements. A $40\times$ aspherical objective lens (Newport 5722-B-H, NA = 0.6) and a plano-convex lens (Thorlabs LA1979-B, focal length 200 mm) image the output facet of the BAL with $40\times$ magnification in the plane where its emission is collected with a MMF (Thorlabs M116L02, see Appendix A 2). An optical isolator (Thorlabs IO-5-850-VLP) avoids parasitic feedback into the BAL from reflections at the fiber facet. The fiber is mounted on a motorized translation stage

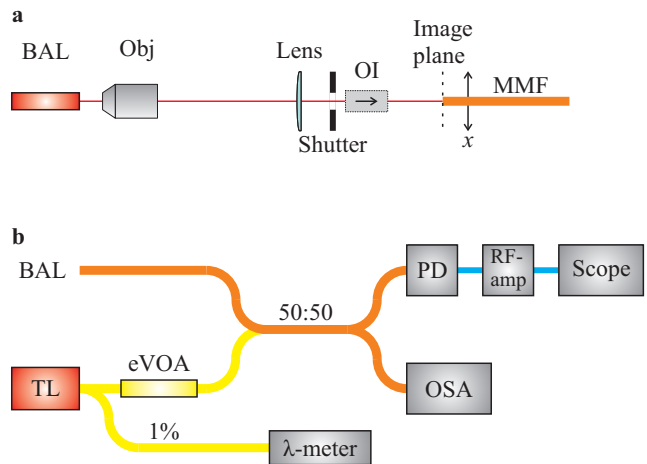


FIG. 7. **Experimental setup for spatially-resolved heterodyne measurements.** **a**, Free-space part of the setup, where x indicates the lateral position of the fiber. BAL: broad-area laser, Obj: $40\times$ objective lens, OI: optical isolator, MMF: multimode fiber. **b**, Fiber-optic part of the setup. Single-mode fibers (multimode fibers) are indicated in yellow (orange), and coaxial cables in blue. TL: tunable laser (reference laser), eVOA: electronic variable optical attenuator, λ -meter: wavelength meter, PD: fast photodetector, RF-amp: RF-amplifier, OSA: optical spectrum analyzer, scope: oscilloscope

(Thorlabs NRT100/M with driver BSC201) and scans the transverse position on the output facet of the BAL with a step size of $20\ \mu\text{m}$ (141 positions). The corresponding step size on the BAL output facet, $0.5\ \mu\text{m}$, is slightly smaller than the spatial resolution of $0.7\ \mu\text{m}$ estimated from the NA of the objective lens.

The signals from the BAL and the reference laser (tunable laser Toptica DL pro with Diode AR 860 nm) are superimposed via a multimode fiber-optic coupler (Thorlabs TM50R5F2B) on a fast photodetector and measured with an oscilloscope (see Appendix A 2). The optical powers of the reference laser and the BAL on the photodetector are adjusted to about 0.75 mW and 0.5 mW, respectively, using a neutral density filter and a variable optical attenuator (VOA), though the power of the BAL can be smaller for low pump currents. The reference laser is set to 20°C with 143 mA pump current and its wavelength adjusted to the desired value. It is left to stabilize for at least 20 min, and we check that it is in a stable single-mode lasing regime. Its wavelength is monitored using a wavelength meter (High Finesse Angstrom WS6-600 IRVIS) connected via a 99 : 1 fiber coupler (Thorlabs TW850R1A2).

At each position of the collection fiber, both the heterodyne signal (reference laser and BAL) and the signal of the BAL alone are measured, so its spatially-resolved RF-spectrum is measured in parallel. Furthermore, the background signals of the reference laser and the photodetector itself were measured. A mechanical shutter

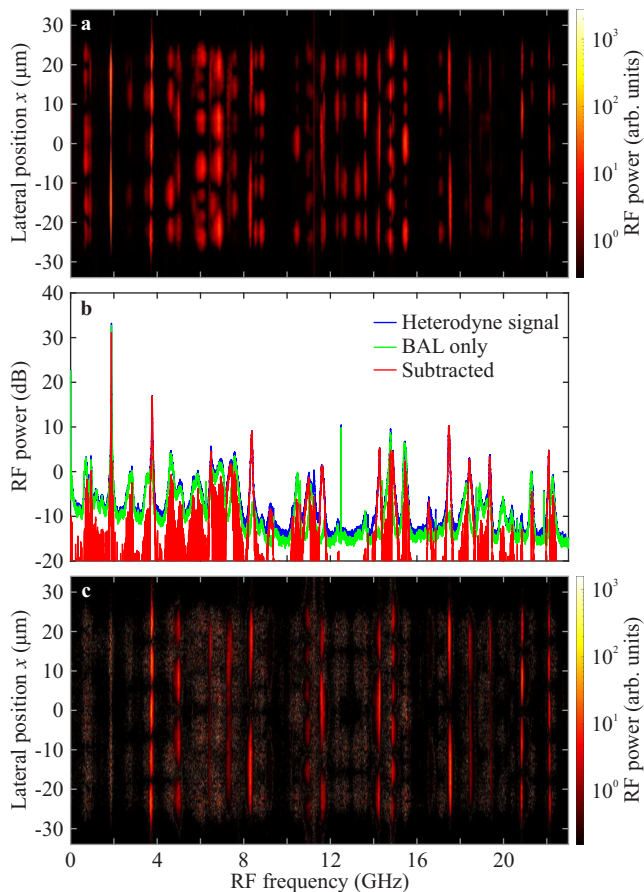


FIG. 8. **Subtraction of BAL-signal in heterodyning measurements.** **a**, RF-spectra of the heterodyne signals as function of the lateral position x . **b**, The RF-spectrum of the BAL alone (green) is subtracted from that of the heterodyning signal (blue) to obtain the subtracted RF-spectrum (red) analyzed in the following (example for $x = 15 \mu\text{m}$). **c**, The subtracted RF-spectra only display the beat notes between BAL and reference laser. The data shown is for a pump current of 400 mA and a reference wavelength of 851.142 nm.

(Thorlabs SH05/M) and an electronic fiber VOA (Thorlabs V800F controlled by a LeCroy Wavestation 3162 signal generator) are used to block the signals of the BAL and the reference laser, respectively, when required. The whole measurement is repeated for a second reference wavelength (shifted by about 0.5 GHz). The complete measurement takes about $4\frac{1}{2}$ min. Measurements are made for pump currents from 300–1000 mA in steps of 50 mA, with six measurements for somewhat different reference wavelengths at each pump current, yielding 90 measurements in total.

2. Analysis of heterodyne measurements

Figure 8 shows the RF-spectra of the heterodyning signals for 400 mA pump current, obtained from the

measured time traces via Fourier transform (see Appendix A 2), which contain both the beat notes between the lasing modes of the BAL and the reference laser and frequency components of the BAL itself. Hence, the RF-spectrum of the signal from the BAL alone is calculated and subtracted as shown in Fig. 8b. It should be emphasized that the RF-power is subtracted in linear scale, not in logarithmic scale which would mean dividing the RF-spectra. In the subtracted RF-spectrum presented in Fig. 8c, the only strong signals left are those of the beat notes between BAL and reference laser, though some residues of the frequency components stemming from the BAL alone still remain. From Fig. 8c we can deduce the spatial profiles of the lasing modes and the beat note frequencies. Since the beat note frequency f_m of mode m with optical frequency is ν_m is $f_m = |\nu_m - \nu_{r,1}|$, where $\nu_{r,1}$ is the optical frequency of the reference laser, we cannot obtain ν_m from Fig. 8c without additional information.

A second measurement with a slightly shifted wavelength (optical frequency $\nu_{r,2}$) of the reference laser allows us to determine the ν_m unambiguously as explained in Fig. 9. When $\nu_m < \nu_{r,1}$ ($\nu_m > \nu_{r,1}$), the optical frequency of mode m is given by $\nu_m = \nu_{r,1} - f_m$ ($\nu_m = \nu_{r,1} + f_m$). Figure 9 shows the resulting spectra for both cases ($\nu_m < \nu_{r,1}$ in the left column and $\nu_m > \nu_{r,1}$ in the right column) and for both reference wavelengths, where the reference for calculating the relative optical frequency is $\nu_{r,1}$ in all cases. If the hypothesis that $\nu_m < \nu_{r,1}$ ($\nu_m > \nu_{r,1}$) is correct, then mode m must appear at the same relative frequency in both spectra to the left (right). These modes are marked by the green arrows in each column. This procedure allows to unambiguously determine the mode frequencies ν_m , even in the presence of "degenerate" modes with the same f_m but different ν_m . Moreover, any residues from the imperfect subtraction of the BAL signals are easily identified as such since they do not appear at the same relative frequency in either column.

The mode frequency $\nu_{m,x}$ for each lateral position x is determined as the center of mass (COM) in a 300 MHz wide frequency window around the estimated mode frequency. In a second step the spatial average weighted with the mode amplitude $A(x)$ for each x is calculated, $\nu_m = \sum_x A(x)\nu_{m,x} / \sum_x A(x)$, and finally the average over the two measurements with different reference laser wavelengths. The spatio-spectral images (Figs. 2a and 3a) are reconstructed by using the spatial profiles obtained from one of the two measurements with different reference wavelength, the averaged mode frequency ν_m and a Lorentzian lineshape with 100 MHz linewidth for the sake of simplicity. The amplitudes of all modes are normalized to one to ensure good visibility of all modes.

While the spectral resolution of the heterodyne measurement is limited only by the linewidth of the reference lasers (< 1 MHz), the actual measurement accuracy of the mode frequencies ν_m is not as good. Fluctuations in the data during the measurement such as slight drifts of the reference laser wavelength or small changes in the

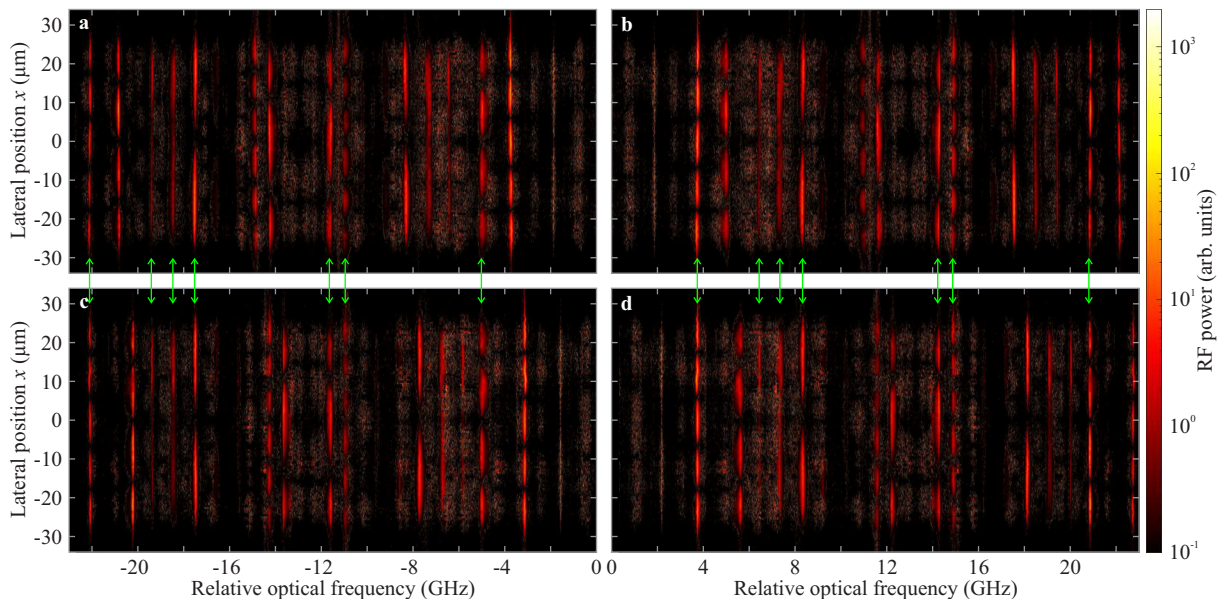


FIG. 9. **Determination of the optical frequencies of lasing modes.** Comparison of measurements with reference wavelength $\lambda_{r,1} = 851.142$ nm (top panels **a**, **b**) and $\lambda_{r,2} = 851.141$ nm (bottom panels **c**, **d**) at 400 mA. The optical frequency is given with respect to $\lambda_{r,1}$ in all panels. The spectra in the left column were calculated assuming that the lasing modes have longer wavelengths than the reference laser, and the spectra in the right column assuming they have shorter wavelengths. The green arrows indicate the modes that appear at the same relative optical frequency for both reference wavelengths.

BAL state manifest as variations of $\nu_{m,x}$. These variations are typically of the order of 10 MHz, which determines the accuracy with which $\nu_m - \nu_r$ is measured. The measurement accuracy of ν_m is limited by the absolute accuracy of ν_r , which is measured by the wavelength meter with a precision of 600 MHz. Finally, it should be noted that the spectral range of the heterodyne measurement is limited by the detection bandwidth of photodetector and oscilloscope which is 23 GHz, yielding a spectral range of 46 GHz (111 pm).

Appendix C: Analysis of linewidths and mode spacings

1. Linewidth determination

The linewidths of peaks in the RF-spectra of the BAL or the heterodyne signals are determined by fitting a Lorentz function,

$$L(f) = A \frac{\Gamma^2}{(f - f_0)^2 + \Gamma^2/4}, \quad (\text{C1})$$

where f_0 is the peak frequency, Γ the full width at half maximum (FWHM), and A the amplitude. In the case of spatially resolved data, a fit is made for each lateral position x , and the linewidth is averaged over x after removing outliers and unsuitable data points. Data points are removed if (i) the fit algorithm did not converge, (ii) the fitted FWHM is unusually small or large, or (iii) the

amplitude is small, which indicates low signal strength and hence unreliable fits. Criterion (ii) means that the linewidth is two times larger or smaller than the median linewidth. Criterion (iii) means that the fitted amplitude A is smaller than the highest fitted amplitude divided by ten.

The linewidth of the beat note between a lasing mode of the BAL and the reference laser is the sum of the two respective mode linewidths since the BAL and the reference laser are completely uncorrelated (see Appendix D1). Since the linewidths of the BAL lasing modes are of the order of 100 MHz, whereas the linewidth of the reference laser is < 1 MHz, the latter is negligible in practice, and we approximate the linewidth of the lasing mode to be equal to the linewidth of the heterodyne beat note.

2. The narrow beat note in the RF-spectra

The broad-area laser investigated here features one narrow peak in the RF-spectrum that is related to multiplets of 1st- and 2nd-order modes (see Fig. 1b). Figure 10 shows the frequency and linewidth of this peak for five different temperatures. Both frequency and linewidth have a complicated dependency on the pump current, and the peak frequency does not exhibit the square-root scaling expected for the relaxation oscillation frequency. The linewidth of the beat note is smallest in the current region of 250 to 650 mA and increases rapidly for higher pump

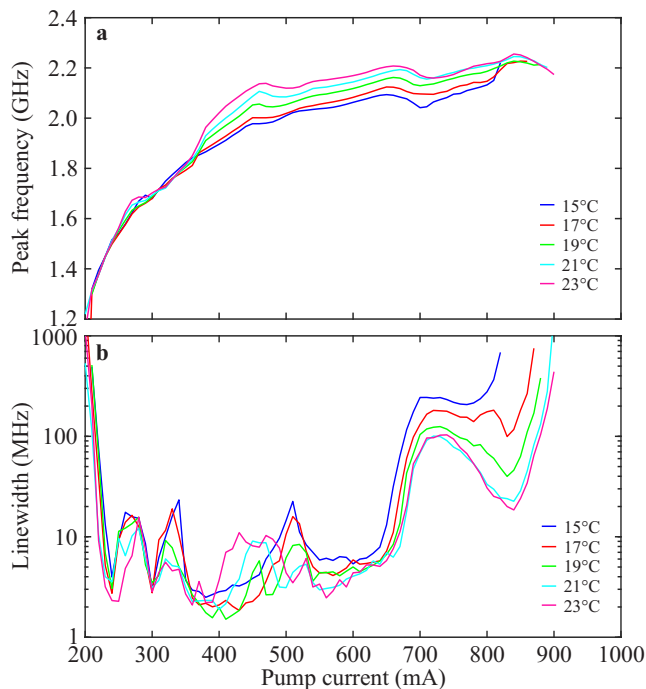


FIG. 10. **Properties of the narrow beat note.** **a**, Frequency of the narrow beat note in the RF-spectrum and **b** its linewidth as function of the pump current for five different set temperatures of the laser diode mount. All measurements were made with laser A.

currents, indicating the loss of phase locking. This is also the regime where the multiplets are observed. Both the peak frequency and linewidth exhibit a number of local extrema and sudden slope changes. These indicate that the nonlinear dynamics creating the multiplets and the phase locking depends sensitively on the pump current, possibly in the context of gain competition between an increasing number of transverse and longitudinal modes.

Both the peak frequency and linewidth depend on the temperature. Figure 10 shows data for five different set temperatures of the laser diode mount ranging from 15°C to 23°C, where 21°C is the default temperature used for all other measurements. However, the effect of temperatures changes on both frequency and linewidth is relatively small. Moreover, the positions of extrema and sudden slope changes are almost the same for different temperatures. This demonstrates that the significant changes of the peak properties as function of the pump current are mainly due to changes in gain and mode competition rather than temperature changes induced by increased Joule heating.

We furthermore test a second laser of the same model, called laser B in the following to distinguish it from laser A for which all other data shown in the article is measured. The RF-spectra of laser B are presented in Fig. 11a, which are qualitatively similar to those of laser A (see Fig. 1a). Most importantly, laser B also exhibits a narrow peak in the RF-spectrum just like laser

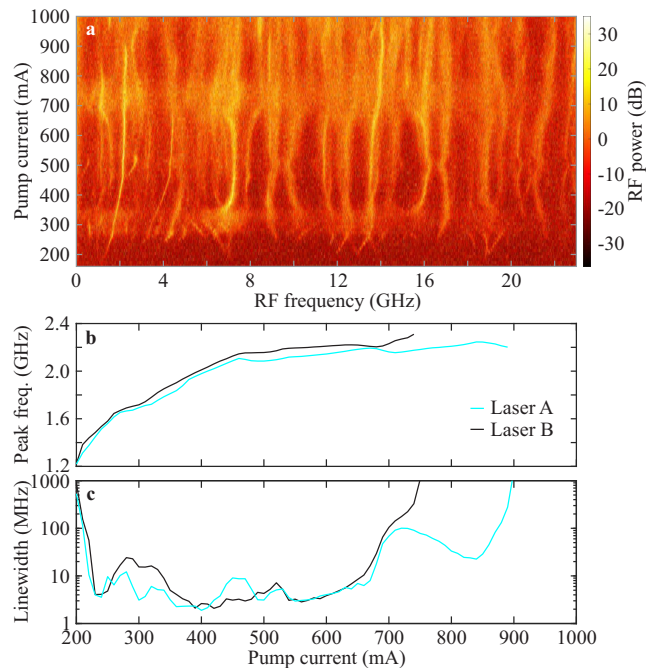


FIG. 11. **Dynamics of laser B.** **a**, RF-spectra of the total laser emission for laser B. **b**, Peak frequency and **c** linewidth of the narrow RF-peak. The data for laser A (cyan) and laser B (black) are compared. All measurements are for a set temperature 21°C.

A. The frequency and linewidth of the narrow peak of laser B are compared to that of laser A in Figs. 11b and c, showing almost quantitative agreement in the current range up to 700 mA. Please note that the data for laser B stops around 750 mA because the Lorentz fit used to determine the linewidth fails for higher pump currents even though the peak is still visible in the RF-spectrum till about 900 mA. These results demonstrate that the phase-locking effect can be found for different lasers of the same model. Thus, the phase locking is reproducible and appears to be typical for certain types of broad-area semiconductor lasers.

3. Spacings and linewidths of the multiplet modes

The nearest-neighbor (NN) spacings of the modes in the multiplets are generally different from the next-nearest-neighbor (NNN) spacings divided by two as shown in Fig. 12. This means that the modes in the multiplets are not equidistant and hence not created by four-wave mixing. It should also be noted that the NN-spacings of different multiplets at the same pump current are not necessarily the same. The NN-spacings increase with pump current, and at the same time the NNN-spacing (and thus the frequency of the narrow beat note) increases as well, so the NNN-spacing remains roughly equal to two times the NN-spacing.

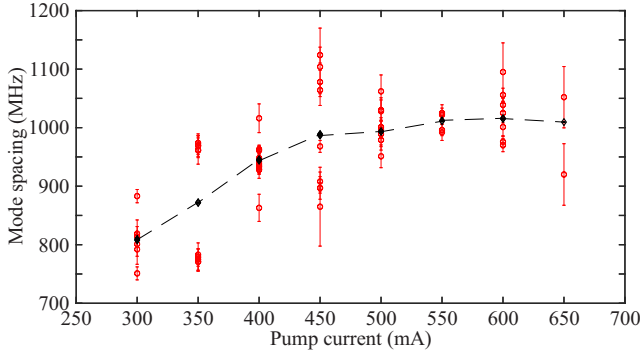


FIG. 12. **Mode spacings in the multiplets.** The NN-spacings (red) are compared to 1/2 the NNN-spacings (black).

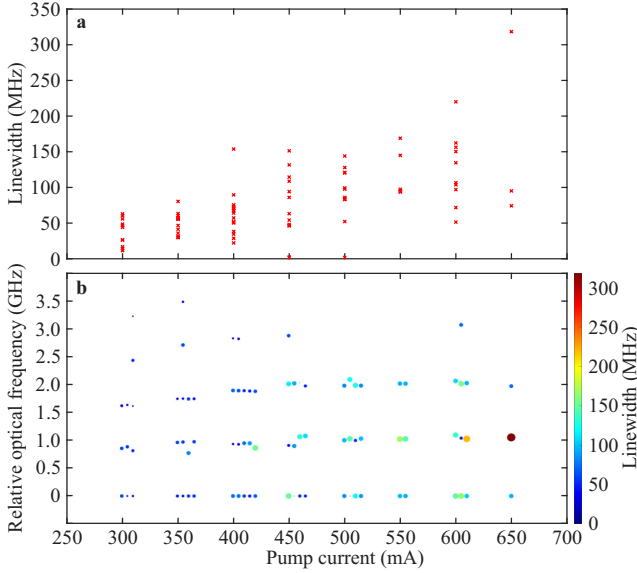


FIG. 13. **Linewidths of the multiplet modes.** **a**, Linewidths as function of the pump current. **b**, Mode linewidths organized by multiplet. The size and the color of the circles corresponds to the linewidth. Different multiplets for the same pump current are offset laterally for clarity.

Figure 13a shows a general increase of the linewidths of the multiplet modes with pump current. It should be noted that the two data points with almost zero linewidth at 450 and 500 mA are artifacts in cases where the Lorentz fit fails, and the mode frequencies are not reliable either in these cases. Since the linewidth of the beat note stays roughly constant around 10 MHz in this current regime, the linewidth reduction factor (LRF) increases as well (see Fig. 3e). So increasing the pump current results in both an increase in the mode linewidth and in the strength of phase locking.

Figure 13b shows the linewidths for each multiplet separately, where multiplets for the same pump current are slightly offset for clarity. We systematically observe that every second mode in the multiplets is broader than its

neighbors as also shown in Fig. 3b.

Appendix D: Phase fluctuations and correlations

1. Theory of linewidth and phase fluctuations

In the following we discuss how the linewidths of lasing modes and beat signals on a photodetector are related to the phase fluctuations of the involved lasing modes, and how information on possible correlations due to phase locking can be extracted. Following Ref. [60], we neglect amplitude fluctuations of the lasing modes and only consider their phase fluctuations.

We will use the following notation and relations: we denote with $\tilde{y}(f) = \mathcal{F}[y(t)]$ the Fourier transform \mathcal{F} of a complex-valued function $y(t)$. Then the power spectral density (PSD) of y is

$$S_y(f) = |\tilde{y}(f)|^2 = \mathcal{F}[C_f(\tau)] \quad (\text{D1})$$

according to the Wiener-Khinchin theorem where

$$C_y(\tau) = \langle y^*(t)y(t+\tau) \rangle \quad (\text{D2})$$

is the first order autocorrelation function of y and $\langle \dots \rangle$ denotes the time average. Furthermore, we denote the finite difference (i.e., short-term fluctuation) over time τ of function y as $\delta_\tau y(t) = y(t+\tau) - y(t)$.

First, we consider a single lasing mode m with electric field

$$E_m(t) = A_m e^{i[\omega_m t + \phi_m(t)]} \quad (\text{D3})$$

where ω_m is the optical angular frequency of the mode, A_m its constant amplitude, and its phase $\phi_m(t)$ follows a Wiener process. Its first-order autocorrelation function is

$$C_{E_m}(\tau) = |A_m|^2 e^{i\omega_m \tau} \langle \exp(i\delta_\tau \phi_m) \rangle. \quad (\text{D4})$$

It is commonly assumed that the phase fluctuations $\delta_\tau \phi_m$ are a zero-mean stationary random Gaussian process [60], that is,

$$\delta_\tau \phi_m(t) = \sqrt{2\pi\Gamma_m|\tau|} z_m(t), \quad (\text{D5})$$

where $z_m(t)$ is a Gaussian random variable with zero mean and standard deviation $\sigma_{z_m} = 1$, and Γ_m is the linewidth of the lasing mode as shown in the following. Using the relation

$$\langle \exp(iz) \rangle = \exp[-\langle z^2 \rangle / 2] = \exp[-\sigma_z^2 / 2] \quad (\text{D6})$$

which only holds for a Gaussian random variable z with zero mean, we obtain

$$C_{E_m}(\tau) = |A_m|^2 e^{i\omega_m \tau} e^{-\pi\Gamma|\tau|}. \quad (\text{D7})$$

The Fourier transform (FT) of the autocorrelation function yields the PSD of the electric field of mode m , i.e., its optical spectrum,

$$S_{E_m}(\nu) = |A_m|^2 \frac{1}{\pi} \frac{\Gamma_m/2}{(\nu - \nu_m)^2 + (\Gamma_m/2)^2}, \quad (\text{D8})$$

which is a Lorentz function with linewidth (FWHM) Γ_m at optical frequency $\nu_m = \omega_m/(2\pi)$.

Next we consider the beat signal of two modes m and n on a photodetector. The total electric field is

$$E_t = A_m e^{i[\omega_m t + \phi_m(t)]} + A_n e^{i[\omega_n t + \phi_n(t)]} \quad (\text{D9})$$

with the same assumptions for the phases of the two modes as discussed above. The photocurrent signal j on the detector is $j(t) = rI(t)$ with r the radiant sensitivity and $I = |E_t|^2$ the light intensity. The first-order autocorrelation function of the current is $C_j(\tau) = r^2 C_{E_t}^{(2)}(\tau)$ where

$$C_{E_t}^{(2)}(\tau) = \langle E_t(t) E_t^*(t) E_t(t + \tau) E_t^*(t + \tau) \rangle \quad (\text{D10})$$

is the second-order autocorrelation function of the total electric field and we neglected shot noise. When calculating $C_{E_t}^{(2)}$, terms with an explicit time dependence drop out due to the time average, and we also remove the DC-terms that we are not interested in. This yields

$$C_{E_t}^{(2)}(\tau) = |A_m|^2 |A_n|^2 e^{i\Delta\omega_{mn}\tau} \langle e^{i(\delta_\tau\phi_m - \delta_\tau\phi_n)} \rangle + \text{c.c.} \quad (\text{D11})$$

with $\Delta\omega_{mn} = \omega_m - \omega_n$. The further analysis depends on the properties of the random variable $\delta_\tau\phi_{mn} = \delta_\tau\phi_m - \delta_\tau\phi_n$ where $\phi_{mn} = \phi_m - \phi_n$, that is, if there are correlations between the phase fluctuations of the two modes.

First we consider the case of uncorrelated modes. This is for example the case in heterodyne measurements where the modes of the BAL and the reference laser are of course uncorrelated. In this case we can use that the sum of two independent Gaussian random variables z_1 and z_2 is a Gaussian random variable z_3 whose average is equal to the sum of the averages of z_1 and z_2 and whose variance is equal to the sum of the variances of z_1 and z_2 , that is $\sigma_{z_3}^2 = \sigma_{z_1}^2 + \sigma_{z_2}^2$. Thus, the random variable $\delta_\tau\phi_{mn}$ is Gaussian and has a variance of $2\pi|\tau|(\Gamma_m + \Gamma_n)$, and applying Eq. (D6) yields

$$C_{E_t}^{(2)}(\tau) = |A_m|^2 |A_n|^2 e^{i\Delta\omega_{mn}\tau} e^{-\pi|\tau|(\Gamma_m + \Gamma_n)}. \quad (\text{D12})$$

The corresponding PSD of the photodetector signal (i.e., the RF-spectrum we measure),

$$S_j(f) = r^2 |A_m|^2 |A_n|^2 \frac{1}{\pi} \frac{(\Gamma_m + \Gamma_n)/2}{(f - \Delta\nu_{mn})^2 + (\Gamma_m + \Gamma_n)^2/4}, \quad (\text{D13})$$

is also a Lorentz function, where $\Delta\nu_{mn} = (\omega_m - \omega_n)/(2\pi)$. Hence, the linewidth of a heterodyne beat notes we measure is the linewidth of the BAL mode plus the linewidth of the reference laser. Since the latter is

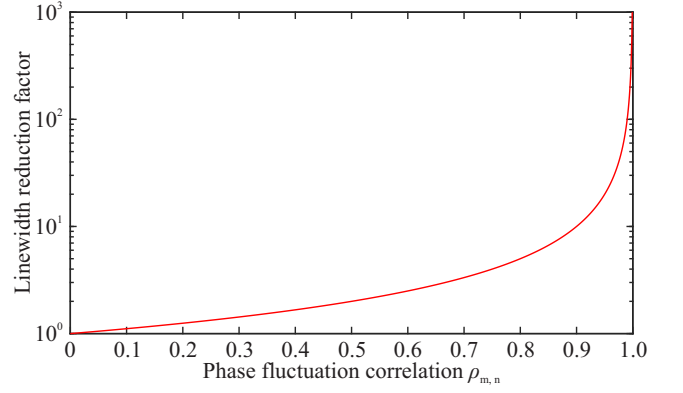


FIG. 14. **Linewidth reduction factor.** The LRF for equal mode linewidths, Eq. (D18), is shown as function of the phase fluctuation correlation $\rho_{m,n}$.

< 1 MHz while the BAL modes have linewidths of 50 MHz and more, the contribution from the reference laser can be neglected in practice.

Next we consider the case of modes with correlated phase fluctuations, such as the NNN-mode pairs in the multiplets. In that case the variance of $\delta_t\phi_{mn}$ is

$$\begin{aligned} \text{Var}(\delta_t\phi_{mn}) &= \text{Var}(\delta_\tau\phi_m) + \text{Var}(\delta_\tau\phi_n) \\ &\quad - 2\text{Cov}(\delta_\tau\phi_m, \delta_\tau\phi_n) \\ &= 2\pi|\tau|(\Gamma_m + \Gamma_n) \\ &\quad - 4\pi|\tau|\sqrt{\Gamma_m\Gamma_n}\text{Cov}(z_m, z_n) \end{aligned} \quad (\text{D14})$$

where $z_{m,n}$ are Gaussian random variables with unit variance [see Eq. (D5)] and Cov denotes the covariance. It should be noted that

$$\text{Cov}(z_m, z_n) = \rho_{z_m, z_n} = \rho_{\delta_\tau\phi_m, \delta_\tau\phi_n} =: \rho_{m,n}, \quad (\text{D15})$$

where $\rho_{x,y}$ is the Pearson correlation coefficient of two variables x and y , and $\rho_{m,n}$ is the phase fluctuation correlation (PFC) of modes m and n .

At this point it should be noted that the sum of two *correlated* random Gaussian variables is not necessarily a Gaussian variable itself. Thus, Eq. (D6) is not guaranteed to be applicable and the lineshape of the beat note not necessarily a Lorentz function. The calculation of the term $\langle e^{i\delta_\tau\phi_{mn}} \rangle$ requires the evaluation of all moments of $\delta_\tau\phi_{mn}$ which include higher-order correlations between $\delta_\tau\phi_m$ and $\delta_\tau\phi_n$. Hence, a careful analysis of the lineshape of the beat note of two phase locked modes could yield information about higher-order phase fluctuation correlations, not just the linear correlation $\rho_{m,n}$. In practice, the narrow beat note in the RF-spectrum is well fitted by a Lorentz function, and measuring the lineshape in greater detail to observe possible deviations from a Lorentz profile is challenging.

For the sake of simplicity we will hence assume that $\delta_\tau\phi_{mn}$ is Gaussian and apply Eq. (D6), yielding a

Lorentzian beat note with linewidth

$$\Gamma_b = \frac{\text{Var}(\delta_\tau \phi_{mn})}{2\pi|\tau|} = \Gamma_m + \Gamma_n - 2\sqrt{\Gamma_m \Gamma_n} \rho_{m,n}. \quad (\text{D16})$$

We define the linewidth reduction factor (LRF) as

$$F_{\text{red}} = \frac{\Gamma_m + \Gamma_n}{\Gamma_b} = \left[1 - 2\frac{\sqrt{\Gamma_m \Gamma_n}}{\Gamma_m + \Gamma_n} \rho_{m,n} \right]^{-1}, \quad (\text{D17})$$

which simplifies to

$$F_{\text{red}} = \frac{1}{1 - \rho_{m,n}} \quad (\text{D18})$$

in the limit of equal mode linewidths, $\Gamma_m \approx \Gamma_n$. Equation (D18) is plotted in Fig. 14 and shows that a LRF of $F_{\text{red}} = 10$ corresponds to phase fluctuation correlation of $\rho_{m,n} = 0.9$.

Finally we consider how the phase fluctuation correlations (PFCs) of two laser modes m and n can be determined from the heterodyne signals, that is, their beat notes with the reference laser r . The intensity of the beat notes between mode m and the reference laser is

$$I_m(t) = 2\text{Re}[A_m A_r \cos(\Delta\omega_{mr} t + \phi_{mr})], \quad (\text{D19})$$

where we removed the DC-terms which our photodetector filters out. We apply the Hilbert transform \mathcal{H} to obtain the analytic signal

$$P_m + i\mathcal{H}[P_m] = 2A_m A_r \exp\{i(\Delta\omega_{mr} t + \phi_{mr})\} \quad (\text{D20})$$

from which we extract the instantaneous amplitude,

$$A_{mr}(t) = |P_m + i\mathcal{H}[P_m]| = 2A_m A_r, \quad (\text{D21})$$

and the instantaneous phase,

$$\theta_{mr}(t) = \arg[P_m + i\mathcal{H}[P_m]] = \Delta\omega_{mr} t + \phi_{mr}(t). \quad (\text{D22})$$

The relative phase of mode m and the reference laser is obtained as

$$\phi_{mr}(t) = \theta_{mr}(t) - \left\langle \frac{d\theta_{mr}}{dt} \right\rangle_t \quad (\text{D23})$$

where we estimate $\Delta\omega_{mr}$ as the average of the numerical derivative of θ_{mr} . From that we obtain the relative phase fluctuations

$$\delta_\tau \phi_{mr}(t) = \sqrt{2\pi|\tau|} \left(\sqrt{\Gamma_m} z_m(t) - \sqrt{\Gamma_r} z_r(t) \right) =: \delta\phi_m \quad (\text{D24})$$

that we denote as $\delta\phi_m$ in the following. In practice, $\tau = 20$ ps is the sampling time step of the oscilloscope, and $\delta\phi_m$ is dominated by the phase fluctuations of the lasing mode since its linewidth Γ_m is much larger than Γ_r .

The same procedure is applied to the beat note of mode n and the reference laser, yielding $\delta\phi_n$. Then we calculate the Pearson correlation coefficient of the two relative phase fluctuations,

$$\rho_{\delta\phi_m, \delta\phi_n} = \frac{\mathcal{E}[\delta\phi_m \delta\phi_n]}{\sigma_{\delta\phi_m} \sigma_{\delta\phi_n}}, \quad (\text{D25})$$

where \mathcal{E} denotes the expectation value. Since the two lasing modes and the reference laser are uncorrelated, we find $\sigma_{\delta\phi_{m,n}} = \sqrt{2\pi|\tau|(\Gamma_{m,n} + \Gamma_r)}$. The product of the relative phase fluctuations in the nominator is

$$\delta\phi_m \delta\phi_n = 2\pi|\tau| \left(\Gamma_r z_r^2 + \sqrt{\Gamma_m \Gamma_n} z_m z_n - \sqrt{\Gamma_m \Gamma_r} z_m z_r - \sqrt{\Gamma_n \Gamma_r} z_n z_r \right). \quad (\text{D26})$$

When we calculate its expectation value, the last two terms vanish since lasing modes and reference laser are uncorrelated, whereas $\mathcal{E}[z_m z_n] = \rho_{m,n}$, which yields

$$\rho_{\delta\phi_m, \delta\phi_n} = \frac{\Gamma_r + \sqrt{\Gamma_m \Gamma_n} \rho_{m,n}}{\sqrt{\Gamma_m + \Gamma_r} \sqrt{\Gamma_n + \Gamma_r}}. \quad (\text{D27})$$

Again we simplify by assuming that $\Gamma_m \approx \Gamma_n$ to obtain

$$\rho_{\delta\phi_m, \delta\phi_n} = \frac{1}{1 + \gamma} + \frac{\gamma}{1 + \gamma} \rho_{m,n} \quad (\text{D28})$$

with $\gamma = \Gamma_m/\Gamma_r$. Thus, the phase fluctuation correlation of the two beat notes has an offset of $1/(1 + \gamma)$ stemming from the phase fluctuations of the reference laser which are present in both beat notes. However, this effect is again negligible for the lasing mode linewidths considered here, so we find $\rho_{\delta\phi_m, \delta\phi_n} \approx \rho_{m,n}$ in good approximation.

So in principle we can determine the PFC $\rho_{m,n}$ of two lasing modes from the correlation of the phase fluctuations of the two heterodyne signals. In practice, the beat note signals of the two modes must be extracted from the measured heterodyne time traces using a relatively narrow frequency filter due to the presence of many other beat notes, and this filter modifies the phase fluctuations and reduces their correlations as discussed in the next section.

We conclude this section with a remark why one should consider the correlation between the phase fluctuations $\delta_\tau \phi_{m,n}(t)$ and not that between the phases $\phi_{m,n}(t)$ themselves. Following Eq. (D5), the phase $\phi_m(t)$ is a sum over many realizations of a Gaussian random variable $z_m(t)$, in other words, the phase performs a one-dimensional random walk. However, it is well known that two random walks can show high (positive or negative) correlations even if the Gaussian variables generating the two random walks are completely uncorrelated [61, 62]. These correlations are spurious in the sense that there is no mathematical or physical reason attached to them. The spurious correlations persist even for arbitrarily long time series [62]. This phenomenon can be explained as follows: a typical random walk with M steps will have a total displacement proportional to \sqrt{M} either in positive or negative direction. Consequently, two random walks going in the same (opposite) direction will show a high correlation (anti-correlation), whereas low correlations are rarely found because only few random walks have a total displacement close to zero. Hence, for random-walk like time series it is good practice to consider the fluctuations around their mean behavior instead when searching for possible correlations [61].

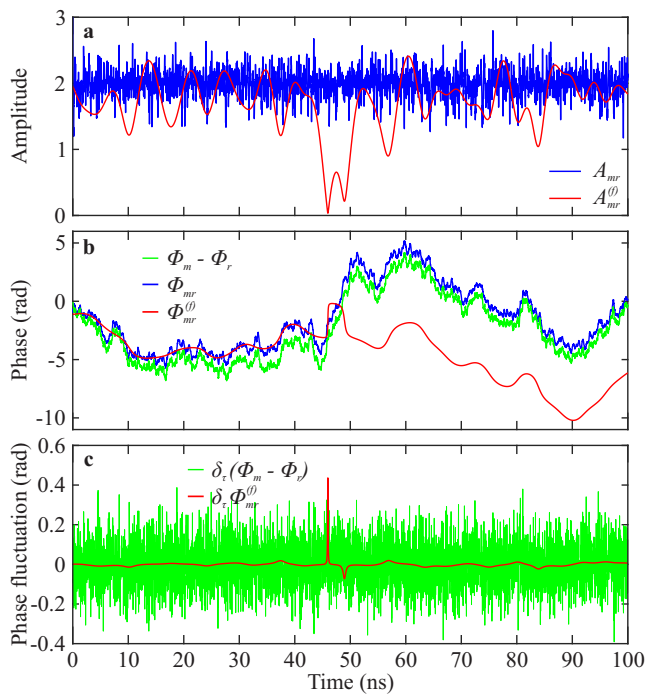


FIG. 15. **Analysis of simulated beat note signal.** **a**, Amplitude of the analytic signal of the simulated beat note without filter (A_{mr} , blue) and with filter ($A_{mr}^{(f)}$, red). **b**, Phase extracted from the simulated beat note without filter (ϕ_{mr} , blue) and with filter ($\phi_{mr}^{(f)}$, red) as well as the original phase ($\phi_m - \phi_r$, green). **c**, Original phase fluctuations ($\delta_\tau(\phi_m - \phi_r)$, green) and phase fluctuations extracted with filter ($\delta_\tau\phi_{mr}^{(f)}$, red).

2. Simulations

In this section we present simulations of a heterodyning signal in order to demonstrate how the phase fluctuations can be extracted from it and to understand the effect of applying a frequency filter. We numerically calculate a heterodyning beat note $I_m(t)$ as in Eq. (D19) with a time step of $\tau = 20$ ps where we choose constant mode amplitudes $A_m = A_r = 1$, a beat note frequency $\Delta\omega_{mr} = 2$ GHz, and linewidths of $\Gamma_m = 100$ MHz and $\Gamma_r = 1$ MHz for the lasing mode and the reference laser, respectively. The phases ϕ_m and ϕ_r of lasing mode and reference laser are calculated as in Eq. (D5). The beat note I_m is a sinusoidal signal with phase modulated by the phase fluctuations of the two lasing modes.

First, we apply the Hilbert transform directly to $I_m(t)$ and extract the amplitude $A_{mr}(t)$ and the phase $\phi_{mr}(t)$ of the beat note as in Eqs. (D21)–(D23). The amplitude shown as blue line in Fig. 15 exhibits small fluctuations around 2 even though it is expected to be constant and equal to 2. Figure 15b compares the phase $\phi_{mr}(t)$ (blue) extracted from the analytic signal to the original phase $\phi_m - \phi_r$ (green) used to calculate the beat note, which agree very well. This demonstrates that the procedure

outlined above allows us to determine the phase fluctuations of the lasing modes from the beat notes, even though there are small deviations between extracted amplitude and phase compared to the simulated ones.

However, in practice the measured heterodyne signals contain several beat notes as well as contributions from the BAL itself, hence a relatively narrow filter must be applied around the individual beat notes in order to separate them from the other signals. To test the effect of filtering, we apply a 300 MHz wide filter [cf. Eq. (D31) below] to the simulated beat note $I_m(t)$. Then we calculate the analytic signal of the filtered time trace $I_m^{(f)}$ and extract amplitude $A_{mr}^{(f)}$ and phase $\phi_{mr}^{(f)}$ as above, which are shown in red in Fig. 15. The amplitude of the filtered signal shows severe fluctuations, including dips going to almost zero. These fluctuations are artifacts induced by the filter: in the event of very fast phase changes, for example at 46 ns in Fig. 15b, the instantaneous frequency of the beat note can leave the frequency range of the filter, thus reducing the amplitude of the filtered signal. This unfortunately means that our heterodyne analysis does not allow us to determine a possible fast amplitude dynamics of the lasing modes since any genuine fluctuations of the amplitude will be obscured by the spurious amplitude fluctuations due to the filter.

The phase (Fig. 15b) is also affected by the filter. First, it is smoothed because very fast phase fluctuations are filtered out. Hence the phase fluctuations of the filtered signal $\delta_\tau\phi_{mr}^{(f)}$ (red line in Fig. 15c) are much smaller than the original ones (green line) and are also smooth, not randomly fluctuating like the original ones. Second, strong dips in the amplitude lead to spurious fluctuations of the phase (phase slips) like at 46 ns where $\phi_{mr}^{(f)}$ no longer follows the original phase. These phase slips manifest in strong extrema of the phase fluctuations. Once the amplitude has recovered (from 55 ns on), the filtered phase once again follows the original one, but with an offset. In order to remove these spurious phase fluctuations induced by the filter, 4 ns long windows around local minima of the amplitude are cut out from the phase fluctuation time traces before calculating their correlation.

Finally we investigate how the data analysis procedure affects the correlation measurement. To this end, we calculate the beat note I_n of another lasing mode n with the reference laser. Lasing modes n and m have the same linewidth of 100 MHz, but we now introduce a correlation ρ_0 of their phase fluctuations. The phase fluctuations of mode n are calculated from the random variable z_n [see Eq. (D5)] given by

$$z_n = \rho_0 z_m + \sqrt{1 - \rho_0^2} z_3, \quad (\text{D29})$$

where z_m and z_3 are independent Gaussian random variables with unit variance. By construction, $\rho_{z_m, z_n} = \rho_0$. We calculate the Pearson correlation coefficient $\rho_{m,n}^{(f)}$ of the filtered phase fluctuations $\delta_\tau\phi_{mr}^{(f)}$ and $\delta_\tau\phi_{nr}^{(f)}$, after additionally removing the parts near local minima of the

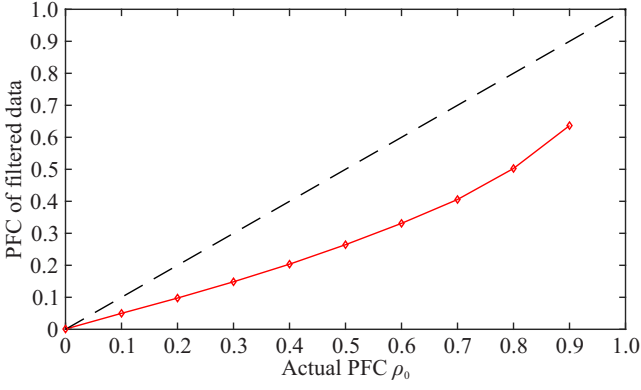


FIG. 16. **Phase fluctuation correlations $\rho_{m,n}^{(f)}$ of filtered beat notes.** The black dashed lines indicates ρ_0 as visual reference.

amplitude as described above. The resulting correlations $\rho_{m,n}^{(f)}$ are compared to the actual correlations ρ_0 of the simulated phase fluctuations in Fig. 16. We find that for small ρ_0 , the extracted PFCs are $\rho_{m,n}^{(f)} \simeq \rho_0/2$ and remain significantly lower even for high ρ_0 . In conclusion, the analysis procedure used to measure the PFCs yields values that are systematically lower than the actual correlations, which partially explains the relatively low PFCs observed experimentally. Nonetheless, our simulations demonstrate that we obtain qualitatively correct information about possible phase correlations between different lasing modes.

3. Analysis of experimental data

First, the heterodyne signals of individual lasing modes are extracted by applying a Fourier filter. The Fourier transform \mathcal{F} of the heterodyne time trace $U(t, x)$ measured at lateral position x is calculated,

$$\tilde{U}(f, x) = \mathcal{F}\{U(t, x)\}, \quad (\text{D30})$$

where f is the RF-frequency. Since $\tilde{U}(f, x)$ contains contributions from many different beat notes as well as the dynamics of the BAL itself, a filter over a frequency interval $[f_1, f_2]$ around the beat note frequency $f_m = |\nu_m - \nu_r|$ is applied, where ν_m is the optical frequency of the lasing mode m and ν_r that of the reference laser. So the filtered time-domain beat note signal of mode m is

$$U_m^{(f)}(t, x) = \mathcal{F}^{-1}\{\tilde{U}(f, x)[B_{f_1, f_2}(f) + B_{-f_2, -f_1}(f)]\}, \quad (\text{D31})$$

where $B_{f_1, f_2}(t)$ is the boxcar function with unit amplitude over the interval $[f_1, f_2]$. It should be noted that $U_m^{(f)}(t, x)$ contains possible signals from the BAL itself in that frequency range which cannot be subtracted in a meaningful way.

The filter interval for mode m is given by

$$f_{1,2} = f_m \mp 3\Gamma_m/2, \quad (\text{D32})$$

where Γ_m is the full width at half maximum (FWHM) of the beat note averaged over x , $\Gamma_m = \langle \Gamma_{m,x} \rangle_x$. Here, the FWHM $\Gamma_{m,x}$ at position x is obtained from the smoothed RF-spectrum of the heterodyne signal,

$$P_{hd}(f, x) = \mathcal{M}\{|\tilde{U}(f, x)|^2\} \quad (\text{D33})$$

where \mathcal{M} is a moving average with 10 MHz width, by determining the -3 dB points around the peak at f_m . Positions for which the FWHM could not be properly determined due to, e.g., low signal strength, are ignored when calculating Γ_m . A total width of $3\Gamma_m$ for the filter is used as a compromise between the requirements of having a large bandwidth and removing noise and interfering signals as much as possible. For a Lorentzian line shape, the filter thus contains 79.5% of the total RF-power of the beat note signal. In practice, the filter width is of the order of a few 100 MHz.

The beat note $U_m^{(f)}(t, x)$ is a sinusoidal signal with a mean oscillation frequency f_m whose phase is modulated by the phase fluctuations of lasing mode m of the BAL and the reference laser. We apply the Hilbert transform to obtain the corresponding analytic signal and decompose it into the instantaneous amplitude $A_{mr}^{(f)}(t, x)$ and instantaneous phase $\theta_{mr}^{(f)}(t, x)$ such that $U_m^{(f)} = \text{Re}[A_{mr}^{(f)} \exp(i\theta_{mr}^{(f)})]$. The average slope of $\theta_{mr}^{(f)}$ corresponds to the beat frequency f_m , and hence we calculate

$$\phi_{mr}^{(f)} = (\theta_{mr}^{(f)} - 2\pi t f_m) \text{sgn}(\nu_m - \nu_r) \quad (\text{D34})$$

where sgn is the sign function. In the following we consider the phase fluctuations

$$\delta_\tau \phi_{mr}^{(f)}(t, x) = \phi_{mr}^{(f)}(t + \tau, x) - \phi_{mr}^{(f)}(t, x) \quad (\text{D35})$$

where $\tau = 20$ ps is the sampling step of the oscilloscope. The phase fluctuations $\delta_\tau \phi_{mr}^{(f)}(t, x)$ are the difference between the phase fluctuations of the lasing mode and that of the reference laser, where the latter are negligible compared to the former since the linewidth of the reference laser is very small compared to that of the lasing modes in our case.

It should be noted that the standard deviation of $\delta_\tau \phi_{mr}^{(f)}(t, x)$ is significantly reduced compared to that of the actual phase fluctuations due to the filter that is applied. Furthermore, very fast phase fluctuations lead to a high instantaneous frequency that causes the signal to (partially) leave the frequency domain of the filter that is applied (see Fig. 15). In such cases, $\delta_\tau \phi_{mr}^{(f)}$ shows spurious values, and the instantaneous amplitude $A_{mr}^{(f)}$ exhibits a strong dip, as discussed in the previous section. To remove these filter artifacts, 4 ns long pieces of $\delta_\tau \phi_{mr}^{(f)}$ are cut around pronounced dips in the amplitude. Finally, the Pearson correlation coefficient $\rho_{m,n}^{(f)}(x)$ between these reduced versions of $\delta_\tau \phi_m^{(f)}(t, x)$ and $\delta_\tau \phi_n^{(f)}(t, x)$ is calculated. As a consequence of the unavoidable filtering process, the measured phase fluctuation correlations $\rho_{m,n}^{(f)}(x)$ are somewhat lower than the actual ones (see Fig. 16).

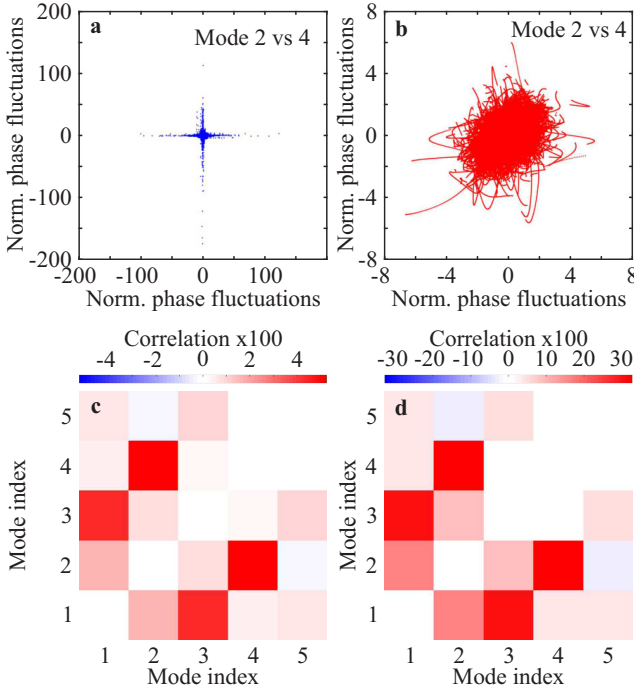


FIG. 17. **Effect of removing phase slips on correlations.** The data is for five modes at 350 mA for lateral position $x = 15 \mu\text{m}$. These are the quintuplet modes shown in Fig. 3. **a**, Correlation diagram for the phase fluctuations $\delta_\tau \phi_{m,r}^{(f)}$ of modes 2 and 4 before removal of the phase slips and **b** after their removal. The phase fluctuations are normalized by their standard deviation. The correlation coefficients are 0.05 and 0.33, respectively. **c**, Correlation matrix of the five modes for $x = 15 \mu\text{m}$ before removal of phase slips and **d** after their removal. Please note the different color scales.

Figure 17 shows how strongly the phase slips that occur as artifacts at local minima of the amplitude affect the measured PFCs. The correlation diagram of two modes of a quintuplet at 350 mA in Fig. 17a has a cross shape which is due to the very strong phase fluctuations that appear during the phase slips. Consequently, the correlation coefficient is only 0.05. By removing 4 ns long windows around the phase slips as described above, these spurious fluctuations are removed, and the correlation diagram becomes an elliptic point cloud with a correlation coefficient of 0.33 as shown in Fig. 17b. The correlation matrices of the quintuplet modes before and after removal of the phase slips are shown in Figs. 17c and d, respectively. The correlations of almost all mode pairs increase drastically when removing the phase slips, and the correlation data shown in Fig. 4 calculated after their removal. Please note that the correlation values in Fig. 17d are different from those in Fig. 4a because the latter includes a spatial average of the PFCs as explained in the following.

Moreover, detector noise and signals from the dynamics of the BAL that fall within the filter bandwidth significantly reduce the measured PFCs as well. The signal-

to-noise ratio of the beat note for mode m at position x is given by

$$\text{SNR}_{m,x} = \max_f \left(\frac{P_{hd}(f,x)}{P_{bal}(f,x)} B_{f_1,f_2}(f) \right) \quad (\text{D36})$$

where the RF-spectrum P_{bal} of the BAL is calculated from its time trace $U_{bal}(t,x)$ in the same way as P_{hd} in Eq. (D33). The joint SNR of the mode pair (m,n) is defined as

$$\text{SNR}_{m,n,x} = (\text{SNR}_{m,x} + \text{SNR}_{n,x})/2, \quad (\text{D37})$$

and the abscissa of Figs. 4b and c is simply $\max_x(\text{SNR}_{m,n,x})$.

Figure 18a and b show the PFC and the signal-to-noise ratio (SNR) of two modes of 1st and 2nd order as function of the lateral position x . Not surprisingly the SNR and in consequence the PFC is low at positions where the modes have low intensities. Figures 18c and d show the correlation diagrams of the PFC and the SNR of the individual modes, which demonstrate how strongly the measured PFCs depend on a good SNR. Hence, we only consider the data points with the best joint SNR, that is,

$$\text{SNR}_{m,n,x} \geq \text{SNR}_{th} = \max_x(\text{SNR}_{m,n,x}) - 5 \text{ dB}. \quad (\text{D38})$$

We calculate $\langle \rho_{m,n}^{(f)} \rangle_x$ as the average of $\rho_{m,n}^{(f)}(x)$ over the data points fulfilling this criterion. The SNR threshold is indicated by the cyan line in Fig. 18b, and the corresponding data points are indicated by cyan dots in Fig. 18a. The average of these data points is $\langle \rho_{2,4}^{(f)} \rangle_x = 0.24 \pm 0.05$ (green line in Fig. 18a).

The example in Fig. 18 is typical for mode pairs with fairly strong correlation and decent SNR. Figure 19 shows the example of a NNN-mode pair at 300 mA which has the highest correlation that was found in the measurement data, $\langle \rho_{4,6}^{(f)} \rangle_x = 0.76 \pm 0.03$. The sum of the linewidths of these lasing modes is 40.7 MHz compared to a linewidth of 9.2 MHz of the beat note, which yields a linewidth reduction factor of $F_{red} = 4.4$. For comparison, the measured PFC of 0.76 corresponds to $F_{red} = 4.14$ according to Eq. (D18), which agrees almost quantitatively. We see in Figs. 19c and d that the PFC saturates with increasing SNR, and it seems that this saturation indicates when the correct value of the PFC is reached. However, it should be noted that this example has an unusually low LRF; in most cases the $F_{red} \geq 10$ (see Fig. 3e), but measuring PFCs above 0.9 appears to be out of reach with the current setup.

4. Comparison to other phase measurement techniques

A commonly used technique to detect phase locking and measuring the relative phases of modes in frequency combs is shifted wave interference Fourier transform spectroscopy (SWIFTS) [55, 56, 63]. However, we

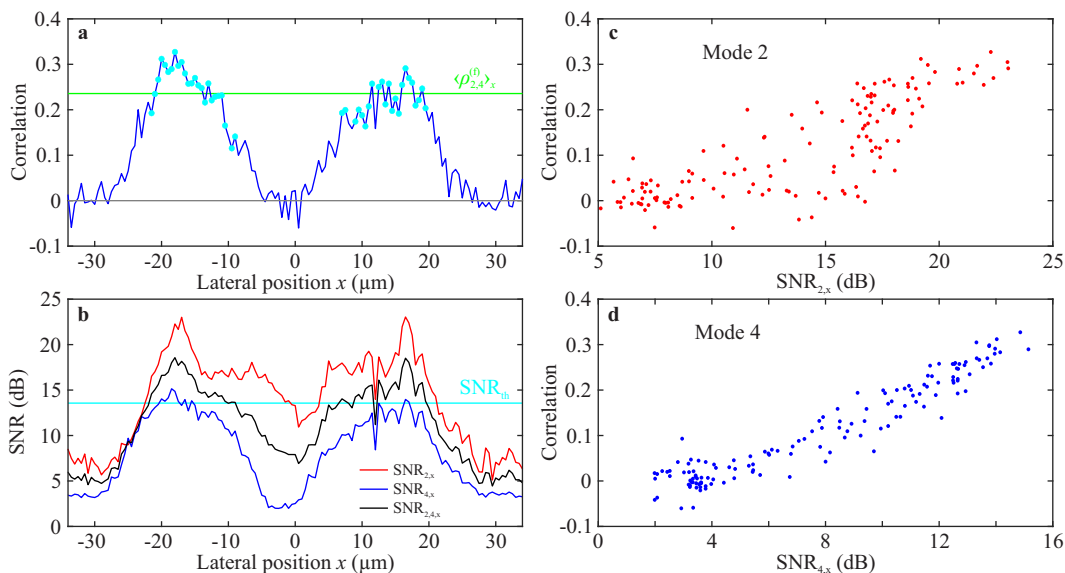


FIG. 18. **Phase fluctuation correlations and SNR, first example.** Data at 350 mA for mode 2 at -11.52 GHz and mode 4 at -9.78 GHz (cf. Fig. 17) is shown. **a**, PFC as function of lateral position x (blue). The data points with a joint SNR above the threshold SNR_{th} are indicated by cyan dots, and their average $\langle \rho_{2,4}^{(f)} \rangle_x = 0.24$ is indicated by the green line. **b**, SNR of modes 2 (red) and 4 (blue) as well as their joint SNR (black) as function of x . The SNR threshold SNR_{th} is indicated by the cyan line. **c**, Correlation diagram between the PFC and the SNR of mode 2 (Pearson correlation of 0.81). **d**, Correlation diagram between the PFC and the SNR of mode 4 (Pearson correlation of 0.96).

cannot use this technique for characterizing our BAL because SWIFTS requires a reference signal with the frequency of the mode spacing, but our laser exhibits many different frequency spacings that are not known *a priori*. Our heterodyne technique is hence more versatile than SWIFTS, in particular for highly multimode lasers and in cases where not all mode pairs are phase locked. On the other hand, its disadvantages are the need for a reference laser which also limits the precision of frequency and phase measurements, a spectral range that is limited to two times the detection bandwidth (2×23 GHz in our case), and the need for a good SNR. Since measuring very high phase correlations correctly is difficult with heterodyning as shown above, our technique is more adapted to detecting weak or partial phase locking like in our BAL, whereas SWIFTS is adapted for strong phase

locking as in the case of frequency combs. Hence heterodyning could be useful, for example, to investigate the transition to mode locking before full coherence between modes is reached.

In Ref. [44] heterodyning was used to investigate mid-infrared and terahertz frequency combs. The main differences of Ref. [44] to our work are that a frequency comb was used as reference laser instead of a single-mode laser as in our case, and both the reference laser and the laser under test were stabilized with a phase-locked loop, whereas we did not use any stabilization. Another difference to SWIFTS and the heterodyne technique in Ref. [44] is that they measure the long-term stability of mode locking, whereas we can consider phase fluctuations on very short time scales, which is more suitable for lasers without additional long-term stabilization.

[1] L. M. Narducci and N. B. Abraham, *Laser Physics and Laser Instabilities* (World Scientific, Singapore, 1988).
 [2] G. H. M. van Tartwijk and G. P. Agrawal, Laser instabilities: a modern perspective, *Prog. Quant. Electron.* **22**, 43 (1998).
 [3] J. Ohtsubo, *Semiconductor Lasers - Stability, Instability and Chaos*, 3rd ed. (Springer, Heidelberg, 2013).
 [4] M. Sciamanna and K. A. Shore, Physics and applications of laser diode chaos, *Nature Photonics* **9**, 151 (2015).
 [5] N. B. Abraham and W. J. Firth, Overview of transverse effects in nonlinear-optical systems, *J. Opt. Soc. Am. B*

7, 951 (1990).
 [6] L. Lugiato, Spatio-temporal structures. part i, *Physics Reports* **219**, 293 (1992).
 [7] G. Huyet, M. C. Martinoni, J. R. Tredicce, and S. Rica, Spatiotemporal dynamics of lasers with a large fresnel number, *Phys. Rev. Lett.* **75**, 4027 (1995).
 [8] C. Jauregui, J. Limpert, and A. Tünnermann, High-power fibre lasers, *Nature Photonics* **7**, 861 (2013).
 [9] Y. Guo, X. Wen, W. Lin, W. Wang, X. Wei, and Z. Yang, Real-time multispeckle spectral-temporal measurement unveils the complexity of spatiotemporal solitons, *Nature*

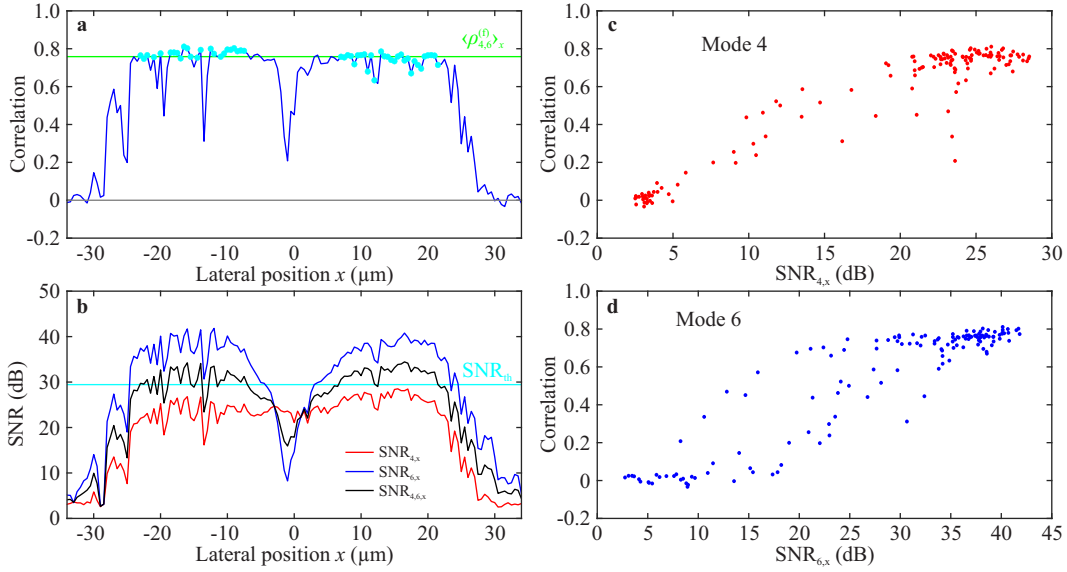


FIG. 19. **Phase fluctuation correlations and SNR, second example.** Data at 300 mA for mode 4 at 14.09 GHz and mode 6 at 15.70 GHz is shown. **a**, PFC as function of lateral position x (blue). The data points with a joint SNR above the threshold SNR_{th} are indicated by cyan dots, and their average $\langle \rho_{4,6}^{(f)} \rangle_x = 0.76$ is indicated by the green line. **b**, SNR of modes 4 (red) and 6 (blue) as well as their joint SNR (black) as function of x . The SNR threshold SNR_{th} is indicated by the cyan line. **c**, Correlation diagram between the PFC and the SNR of mode 4 (Pearson correlation of 0.95). **d**, Correlation diagram between the PFC and the SNR of mode 6 (Pearson correlation of 0.92).

- Comm. **12**, 67 (2021).
- [10] S. Bittner and M. Sciamanna, Complex nonlinear dynamics of polarization and transverse modes in a broad-area vcsel, *APL Phot.* **7**, 126108 (2022).
- [11] M. Giudici, J. R. Tredicce, G. Vaschenko, J. J. Rocca, and C. S. Menoni, Spatio-temporal dynamics in vertical cavity surface emitting lasers excited by fast electrical pulses, *Opt. Comm.* **158**, 313 (1998).
- [12] I. Fischer, O. Hess, W. Elsässer, and E. Göbel, Complex spatio-temporal dynamics in the near-field of a broad-area semiconductor laser, *Europhys. Lett.* **35**, 579 (1996).
- [13] J. R. Marciante and G. P. Agrawal, Spatio-temporal characteristics of filamentation in broad-area semiconductor lasers: experimental results, *IEEE Phot. Tech. Lett.* **10**, 54 (1998).
- [14] D. Scholz, H. Braun, U. T. Schwarz, S. Brüninghoff, D. Queren, A. Lell, and U. Strauss, Measurement and simulation of filamentation in (al,in)gan laser diodes, *Opt. Express* **16**, 6846 (2008).
- [15] L. G. Wright, D. N. Christodoulides, and F. W. Wise, Spatiotemporal mode-locking in multimode fiber lasers, *Science* **358**, 94 (2017).
- [16] L. G. Wright, P. Sidorenko, H. Pourbeyram, Z. M. Ziegler, A. Isichenko, B. A. Malomed, C. R. Menyuk, D. N. Christodoulides, and F. W. Wise, Mechanisms of spatiotemporal mode-locking, *Nature Physics* **16**, 565 (2020).
- [17] S. Bittner, S. Guazzotti, Y. Zeng, X. Hu, H. Yilmaz, K. Kim, S. S. Oh, Q. J. Wang, O. Hess, and H. Cao, Suppressing spatio-temporal lasing instabilities with wave-chaotic microcavities, *Science* **361**, 1225 (2018).
- [18] K. Kim, S. Bittner, Y. Jin, Y. Zeng, Q. J. Wang, and H. Cao, Impact of cavity geometry on microlaser dynamics, *Phys. Rev. Lett.* **131**, 153801 (2023).
- [19] S. B. Ivars, Y. V. Kartashov, P. F. de Córdoba, J. A. Conejero, L. Torner, and C. Milián, Photonic snake states in two-dimensional frequency combs, *Nature Photonics* **17**, 767 (2023).
- [20] C.-W. Chen, K. Wisal, Y. Eliezer, A. D. Stone, and H. Cao, Suppressing transverse mode instability through multimode excitation in a fiber amplifier, *Proc. Nat. Acad. Sci.* **120**, e2217735120 (2023).
- [21] D. M. Abrams and S. H. Strogatz, Chimera states for coupled oscillators, *Phys. Rev. Lett.* **93**, 174102 (2004).
- [22] M. R. Tinsley, S. Nkomo, and K. Showalter, Chimera and phase-cluster states in populations of coupled chemical oscillators, *Nature Physics* **8**, 662 (2012).
- [23] J. Shena, J. Hizanidis, V. Kovanis, and G. P. Tsironis, Turbulent chimeras in large semiconductor laser arrays, *Scientific Reports* **7**, 42116 (2017).
- [24] L. Larger, B. Penkovsky, and Y. Maistrenko, Laser chimeras as a paradigm for multistable patterns in complex systems, *Nature Comm.* **6**, 7752 (2015).
- [25] C.-H. Uy, L. Weicker, D. Rontani, and M. Sciamanna, Optical chimera in light polarization, *APL Phot.* **4**, 056104 (2019).
- [26] E. A. Viktorov, T. Habruseva, S. P. Hegarty, G. Huyet, and B. Kelleher, Coherence and incoherence in an optical comb, *Phys. Rev. Lett.* **112**, 224101 (2014).
- [27] Y. Tanguy, J. Houlihan, G. Huyet, E. A. Viktorov, and P. Mandel, Synchronization and clustering in a multimode quantum dot laser, *Phys. Rev. Lett.* **96**, 053902 (2006).
- [28] D. Kazakov, N. Opačak, F. Pilat, Y. Wang, A. Belyanin, B. Schwarz, and F. Capasso, Cluster synchronization in a semiconductor laser, *APL Phot.* **9**, 026104 (2024).

- [29] O. Hess, Spatio-temporal complexity in multi-stripe and broad-area semiconductor lasers, *Chaos, Solitons & Fractals* **4**, 1597 (1994).
- [30] O. Hess and T. Kuhn, Maxwell-bloch equations for spatially inhomogeneous semiconductor lasers. ii. spatiotemporal dynamics, *Phys. Rev. A* **54**, 3360 (1996).
- [31] H. Adachihara, O. Hess, E. Abraham, P. Ru, and J. V. Moloney, Spatiotemporal chaos in broad-area semiconductor lasers, *J. Opt. Soc. Am. B* **10**, 658 (1993).
- [32] J. Marciante and G. Agrawal, Spatio-temporal characteristics of filamentation in broad-area semiconductor lasers, *IEEE J. Quant. Electron.* **33**, 1174 (1997).
- [33] J. Kaiser, I. Fischer, W. Elsässer, E. Gehrig, and O. Hess, Mode-locking in broad-area semiconductor lasers enhanced by picosecond-pulse injection, *IEEE J. Sel. Top. Quant. Electron.* **10**, 968 (2004).
- [34] J. Kaiser, I. Fischer, , and W. Elsässer, Mode locking of lateral modes in broad-area semiconductor lasers by subharmonic optical pulse injection, *Appl. Phys. Lett.* **88**, 101110 (2006).
- [35] M. Arahata and A. Uchida, Inphase and antiphase dynamics of spatially-resolved light intensities emitted by a chaotic broad-area semiconductor laser, *IEEE J. Sel. Top. Quant. Electron.* **21**, 1800609 (2015).
- [36] T. Tachikawa, S. Takimoto, R. Shogenji, and J. Ohtsubo, Dynamics of broad-area semiconductor lasers with short optical feedback, *IEEE J. Quant. Electron.* **46**, 140 (2010).
- [37] N. Stelmakh and M. Vasilyev, Spatially-resolved self-heterodyne spectroscopy of lateral modes of broad-area laser diodes, *Opt. Express* **22**, 3845 (2014).
- [38] N. Stelmakh and M. Flowers, Measurement of spatial modes of broad-area diode lasers with 1-ghz resolution grating spectrometer, *IEEE Phot. Tech. Lett.* **18**, 1618 (2006).
- [39] P. Crump, S. Böldicke, C. M. Schultz, H. Ekhteraei, H. Wenzel, and G. Erbert, Experimental and theoretical analysis of the dominant lateral waveguiding mechanism in 975 nm high power broad area diode lasers, *Semicond. Sci. Tech.* **27**, 045001 (2012).
- [40] L. Uhlig, D. J. Kunzmann, and U. T. Schwarz, Characterization of lateral and longitudinal mode competition in blue ingan broad-ridge laser diodes, *Phys. Stat. Sol. A* **220**, 0751 (2023).
- [41] W. Elsässer and E. Gobel, Multimode effects in the spectral linewidth of semiconductor lasers, *IEEE J. Quant. Electron.* **21**, 687 (1985).
- [42] D. Brunner, M. C. Soriano, X. Porte, and I. Fischer, Experimental phase-space tomography of semiconductor laser dynamics, *Phys. Rev. Lett.* **115**, 053901 (2015).
- [43] M. J. Wishon, A. Locquet, C. Y. Chang, D. Choi, and D. S. Citrin, Crisis route to chaos in semiconductor lasers subjected to external optical feedback, *Phys. Rev. A* **97**, 033849 (2018).
- [44] F. Cappelli, L. Consolino, G. Campo, I. Galli, D. Mazzotti, A. Campa, P. C. P. Mario Siciliani de Cumis, R. Eramo, M. Rösch, M. Beck, G. Scalari, J. Faist, P. D. Natale, and S. Bartalini, Retrieval of phase relation and emission profile of quantum cascade laser frequency combs, *Nature Photonics* **13**, 562 (2019).
- [45] S. K. Mandre, I. Fischer, and W. Elsässer, Spatiotemporal emission dynamics of a broad-area semiconductor laser in an external cavity: stabilization and feedback-induced instabilities, *Opt. Comm.* **244**, 355 (2005).
- [46] P. W. Smith, Simultaneous phase-locking of longitudinal and transverse laser modes, *Appl. Phys. Lett.* **13**, 235 (1968).
- [47] D. Côté and H. M. van Driel, Period doubling of a femtosecond titanium:sapphire laser by total mode locking, *Opt. Lett.* **23**, 715 (1998).
- [48] M. O. Ziegler, M. Münkel, T. Burkhard, G. Jennemann, I. Fischer, and W. Elsässer, Spatiotemporal emission dynamics of ridge waveguide laser diodes: picosecond pulsing and switching, *J. Opt. Soc. Am. B* **16**, 2015 (1999).
- [49] G.-L. Tan, R. Mand, and J. Xu, Self-consistent modeling of beam instabilities in 980-nm fiber pump-lasers, *IEEE J. Quant. Electron.* **33**, 1384 (1997).
- [50] X. Fu, G. Tan, R. Gordon, and J. Xu, Third-order nonlinearity induced lateral-mode frequency locking and beam instability in the high-power operation of narrow-ridge semiconductor lasers, *IEEE J. Quant. Electron.* **34**, 1447 (1998).
- [51] M. Choi, T. Fukushima, and T. Harayama, Alternate oscillations in quasistadium laser diodes, *Phys. Rev. A* **77**, 063814 (2008).
- [52] H.-Z. Weng, Y.-Z. Huang, X.-W. Ma, F.-L. Wang, M.-L. Liao, Y.-D. Yang, and J.-L. Xiao, Spectral linewidth analysis for square microlasers, *IEEE Phot. Tech. Lett.* **29**, 1931 (2017).
- [53] T. Harayama, T. Fukushima, S. Sunada, and K. S. Ikeda, Asymmetric stationary lasing patterns in 2d symmetric microcavities, *Phys. Rev. Lett.* **91**, 073903 (2003).
- [54] T. Fukushima, T. Tanaka, and T. Harayama, Unidirectional beam emission from strained ingasp multiple-quantum-well quasistadium laser diodes, *Appl. Phys. Lett.* **86**, 171103 (2005).
- [55] A. Hugi, G. Villares, S. Blaser, H. C. Liu, and J. Faist, Mid-infrared frequency comb based on a quantum cascade laser, *Nature* **492**, 229 (2012).
- [56] D. Burghoff, T.-Y. Kao, N. Han, C. W. I. Chan, X. Cai, Y. Yang, D. J. Hayton, J.-R. Gao, J. L. Reno, and Q. Hu, Terahertz laser frequency combs, *Nature Photonics* **8**, 462 (2014).
- [57] N. Yu, L. Diehl, E. Cubukcu, D. Bour, S. Corzine, G. Höfler, A. K. Wojcik, K. B. Crozier, A. Belyanin, and F. Capasso, Coherent coupling of multiple transverse modes in quantum cascade lasers, *Phys. Rev. Lett.* **102**, 013901 (2009).
- [58] A. K. Wójcik, N. Yu, L. Diehl, F. Capasso, and A. Belyanin, Self-synchronization of laser modes and multistability in quantum cascade lasers, *Phys. Rev. Lett.* **106**, 133902 (2011).
- [59] T. Asatsuma, Y. Takiguchi, S. Frederico, A. Furukawa, and S. Hirata, Successive phase change and stability of near-field patterns for broad-area laser diodes, *Proc. SPIE* **6104**, 6104C (2006).
- [60] P. Gallion and G. Debarge, Quantum phase noise and field correlation in single frequency semiconductor laser systems, *IEEE J. Quant. Electron.* **20**, 343 (1984).
- [61] C. W. Granger and P. Newbold, Spurious regressions in econometrics, *Journal of Econometrics* **2**, 111 (1974).
- [62] P. C. B. Phillips, Understanding spurious regressions in econometrics, *Journal of Econometrics* **33**, 311 (1986).
- [63] M. Singleton, P. Jouy, M. Beck, and J. Faist, Evidence of linear chirp in mid-infrared quantum cascade lasers, *Optica* **5**, 948 (2018).